JOURNAL OF GEOPHYSICAL RESEARCH, VOL. 106, NO. D6, PAGES 5295–5316, MARCH 27, 2001

Evaluation of aerosol direct radiative forcing in MIRAGE

Steven Ghan,[1] Nels Laulainen,[1] Richard Easter,[1] Richard Wagener,[2] Seth Nemesure,[2] Elaine Chapman,[1] Yang Zhang,[3] and Ruby Leung[1]

Abstract. A variety of measurements have been used to evaluate the treatment of aerosol radiative properties and radiative impacts of aerosols simulated by the Model for Integrated Research on Atmospheric Global Exchange (MIRAGE). The treatment of water uptake in MIRAGE agrees with laboratory measurements, and the growth of aerosol extinction with relative humidity in MIRAGE simulations agrees with field measurements. The simulated frequency of relative humidity near 100% is about twice that of analyzed relative humidity. When the analyzed relative humidity is used to calculate aerosol water uptake in MIRAGE, the simulated aerosol optical depth agrees with most surface measurements after cloudy conditions are filtered out and differences between model and station elevations are accounted for, but simulated optical depths are too low over Brazil and central Canada. Simulated optical depths are mostly within a factor of 2 of satellite estimates, but are too high off the east coasts of the United States and China and too low off the coast of West Africa and in the Arabian Sea. The simulated single-scatter albedo is consistent with surface measurements. MIRAGE correctly simulates a larger Ångström exponent near regions with emissions of submicron particles and aerosol precursor gases, and a smaller exponent near regions with emissions of coarse particles. The simulated sensitivity of radiative forcing to aerosol optical depth is consistent with estimates from measurements. The simulated direct forcing is within the uncertainty of estimates from measurements in the North Atlantic.

1. Introduction

Radiative scattering and absorption of sunlight by aerosols have a measurable impact on the surface and top-of-the-atmosphere radiation balance. This impact is known as the aerosol direct radiative forcing (the indirect forcing involves the role of aerosol particles as cloud condensation nuclei). Surface, aircraft, and satellite measurements have been used to quantify the impact at the surface and top of the atmosphere [*Kaufmann*, 1997; *Hobbs et al.*, 1997; *Francis et al.*, 1999; *Hignett et al.*, 1999; *Russell et al.*, 1999; *Bergstrom and Russell*, 1999]. However, such measurements cannot distinguish between the natural and the anthropogenic component of the aerosol radiative forcing. Physically based models are necessary to separate the natural and the anthropogenic components of the forcing and to consider future scenarios of emissions of aerosols and their precursor gases.

The Pacific Northwest National Laboratory (PNNL) Model for Integrated Research on Atmospheric Global Exchanges (MIRAGE) was developed for such a purpose. It consists of a detailed global tropospheric chemistry and aerosol model that predicts concentrations of oxidants as well as aerosols and aerosol precursors, coupled to a general circulation model that predicts cloud water and cloud ice mass and cloud droplet and ice crystal number concentrations [*Ghan et al.*, 1997a, 1997b]. Both number and mass of several externally mixed lognormal aerosol size modes are predicted, with internal mixing assumed for the different aerosol components within each mode. Predicted aerosol species include sulfate, organic and black carbon, soil dust, and sea salt. The climate model uses physically based treatments of aerosol radiative properties (including dependence on relative humidity) and aerosol activation as cloud condensation nuclei and ice nuclei. More detailed descriptions of the chemistry and aerosol treatment in MIRAGE are presented by R. C. Easter (manuscript in preparation, 2000)(hereinafter referred to as E2000). The treatment of water uptake and aerosol radiative properties are described in section 3 of this paper. *Ghan et al.* [this issue (a)] describe the treatment of cloud-aerosol interactions and cloud radiative properties in MIRAGE.

Before models can be used to estimate the anthropogenic aerosol radiative forcing, they must be thoroughly evaluated. E2000 evaluate the simulation of the concentrations of the aerosols and their precursor gases by MIRAGE. *Ghan et al.* [this issue (a)] evaluate the simulation of the aerosol indirect forcing. In this paper we evaluate the simulation of the aerosol direct forcing by MIRAGE. Note that we do not evaluate the simulation of the direct forcing by anthropogenic aerosol because measurements cannot distinguish natural and anthropogenic aerosol. The focus here is on the total aerosol. *Ghan et al.* [this issue (b)] apply MIRAGE to estimate the direct and indirect forcing by anthropogenic sulfate particles.

2. Evaluation Strategy

Evaluation of the simulated aerosol direct forcing requires measurements of a variety of fields related to aerosol direct forcing. Comparison with measurements of aerosol direct forcing alone provides little information about the causes of

[1]Pacific Northwest National Laboratory, Richland, Washington.
[2]Brookhaven National Laboratory, Upton, New York.
[3]Atmospheric and Environmental Research, San Ramon, California.

Paper number 2000JD900502.
0148-0227/01/2000JD900502$09.00

differences between simulated and measured aerosol radiative forcing. Measurements of aerosol mass concentration, composition, size distribution, and radiative properties in all three spatial dimensions are needed to explain differences between simulated and observed aerosol radiative forcing. Our evaluation strategy is to employ a suite of complementary and redundant measurements to evaluate the aerosol radiative forcing simulated by MIRAGE.

The focus of our evaluation will be on the period August 1994, when a detailed estimate of the aerosol optical depth and radiance was performed using Advanced Very High Resolution Radiometer (AVHRR) satellite measurements [*Wagener et al.*, 1997]. Although most attention is devoted to this period, other periods are also considered to evaluate the full annual cycle of the simulated radiative forcing. MIRAGE was run for the period June 1994 to May 1995 after a spin-up of 3 months. The horizontal resolution is T42 spectral (about 2.8° latitude and longitude) with 24 layers. Nudging toward the European Center for Medium-Range Weather Forecasts (ECMWF) analyzed winds, temperature, and sea surface temperature is applied to permit evaluation on timescales of days to weeks [*Feichter and Lohmann*, 1999]. Nudging reduces the need for multiyear simulations because the simulated circulation systems are constrained to follow those observed.

The evaluation data are selected primarily to coincide with the simulation period. However, in some cases, data for other years are used if data for the simulation period are not available.

3. Evaluation

3.1. Aerosol Water Uptake

One of the most important factors contributing to aerosol direct forcing is water uptake. MIRAGE uses Köhler theory to treat hygroscopic growth. For each aerosol mode we express water uptake in terms of the relative humidity, the mean dry radius, the relative contributions of each component of the aerosol to the total particle hygroscopicity, and the water on the aerosol from the previous time step. We assume that each aerosol mode is composed of an internal mixture of components. The bulk hygroscopicity of the mode B is expressed in terms of the volume-weighted contributions of each component j of the aerosol to the bulk hygroscopicity [*Abdul-Razzak and Ghan*, 2000],

$$B = \sum_{j=1}^{J} B_j q_j / \rho_j \Big/ \sum_{j=1}^{J} q_j / \rho_j , \qquad (1)$$

where $B_j = \nu_j \phi_j \varepsilon_j \rho_j M_w / \rho_w M_j$ is the hygroscopicity of component j, q_j is the mass mixing ratio of component j, ν_j is the number of ions the salt disassociates into, ϕ_j is the osmotic coefficient, ε_j is the soluble mass fraction, M_j is the molecular weight of the aerosol material, ρ_j is the density of component j, ρ_w is the density of water, and M_w is the molecular weight of water.

Table 1 lists values of ν_j, ϕ_j, ε_j, ρ_j, M_j, and B_j for each of the components of the aerosol. The values of ϕ_j and B_j vary with solution strength, but we use a fixed value, appropriate for dilute solutions, to simplify the water uptake calculations. As a result, our water uptake calculations are more accurate at high relative humidity, when aerosol water contents are greatest and less accurate at lower relative humidity. For water uptake calculations, sea-salt aerosol is treated as pure NaCl, neglecting the influence of other salts and organic material on the hygroscopicity and surface tension of the particles. For soil dust, organic carbon, and black carbon, which are not single compounds, not all the parameters are meaningful. Black carbon is treated as essentially insoluble. It is assigned a small nonzero hygroscopicity to avoid computational difficulties, but the resulting water uptake is negligible. For soil dust, we assume water-soluble mass fractions of 0.024, 0.0028, 0.0038, and 0.014 for Ca, K, Mg, and Na, respectively, based on observations of east Asian dust by *Nishikawa et al.* [1991] and *Nishikawa* [1993]. Assuming that these elements are present as carbonate or sulfate salts, we then calculate ε_j and B_j as weighted averages of their values for the water-soluble Ca, K, Mg, and Na salts and the remaining insoluble material.

Organic aerosol is generally a complex mixture of hundreds of individual organic compounds. Detailed chemical analyses of organic aerosol generally identify less than half of the organic aerosol mass, and hygroscopicity information is available for relatively few organic compounds. Thus hygroscopicity of organic aerosol must currently be treated empirically. We rely primarily on measurements and estimates of the humidity dependence of aerosol light scattering efficiency,

$$f_X(\mathrm{RH}) = b_{sp,X}(\mathrm{RH})/b_{sp,X}(Rh_{\mathrm{dry}}) \qquad (2)$$

where $b_{sp,X}(\mathrm{RH})$ is the humidity-dependent light scattering of an aerosol of composition X, and $b_{sp,X}(Rh_{\mathrm{dry}})$ at a low humidity (e.g., 20%) where the aerosol water content is very small. *Sloane* [1986] estimated $f_{TC} / f_{SO_4} \cong 0.6$ at 70-80% RH where f_{TC} and f_{SO_4} are the humidification factors for total carbonaceous and sulfate aerosol, respectively. *Malm et al.*

Table 1. For Each Aerosol Chemical Component, ν (Number of Ions the Salt Disassociates Into), ϕ (Osmotic Coefficient), ε (Soluble Mass Fraction), ρ (Material Density), M (Molecular Weight of Aerosol Material), B (Hygroscopicity), and Refractive Index for Solar and Infrared Wavelengths

Component	ν	ϕ	ε	ρ	M	B	Refractive Index	
							Solar	Infrared
Water				1.00	18		1.33+0.0*i*	1.18+0.68*i*
Ammonium sulfate	3	0.7	1.0	1.77	132	0.51	1.53+0.0*i*	1.98+0.06*i*
MSA	3	0.7	1.0	1.48	96	0.58	1.53+0.0*i*	1.98+0.06*i*
Sea salt	2	1.0	1.0	1.90	59	1.16	1.50+0.0*i*	1.50+0.01*i*
Soil dust	--	--	0.13	2.60	--	0.14	1.50+0.002*i*	1.62+0.12*i*
Organic carbon	--	--	--	1.00	--	0.14	1.55+0.0*i*	1.70+0.07*i*
Black carbon	--	--	--	1.7	--	$5 \cdot 10^{-7}$	1.90+0.60*i*	2.22+0.73*i*

[1994] developed an empirical expression for the humidification factor of organic aerosol f_{OC}, which gives f_{OC}/f_{SO_4}=0.5-0.4 at 80-90% RH. *Kotchenruther et al.* [1999] measured an overall (unspeciated) $f(80\%)$=1.9-2.6 for aerosol consisting of primarily ammonium bisulfate and carbonaceous material; these measurements, in combination with estimates of carbonaceous and sulfate light-scattering efficiencies [*Hegg et al.*, 1997], are consistent with $f_{OC}(80\%)/f_{SO_4}(80\%) \cong 0.5$. *Kotchenruther and Hobbs* [1998] measured overall $f(80\%)$=1.1-1.3 in biomass burning areas in Brazil, suggesting very low water uptake by these biomass smoke aerosols. We have assumed an organic carbon hygroscopcity of 0.14, approximately one-fourth the ammonium sulfate value. This value is consistent with $f_{OC}(80\%)/f_{SO_4}(80\%) \cong 0.5$ in that with B=0.14 and 0.51 for organic carbon and ammonium sulfate, the ratios of aerosol wet volume to dry volume at 80% RH are 1.63 and 3.28, respectively, so the volume increase of organic carbon is one-half that of ammonium sulfate. We recognize the considerable uncertainty associated with this assumption.

The volume-mean dry radius r_d is

$$r_d \equiv \left(\frac{3}{4\pi N} \sum_{j=1}^{J} \frac{q_j}{\rho_j} \right)^{\frac{1}{3}}, \quad (3)$$

where N is the aerosol number mixing ratio. Using Köhler theory [*Pruppacher and Klett*, 1997], the volume-mean wet radius r_w is determined from the solution of

$$\ln(RH) = \frac{A}{r_w} - \frac{Br_d^3}{(r_w^3 - r_d^3)}. \quad (4)$$

The Kelvin effect factor A is defined as

$$A \equiv \frac{2M_w\sigma_{s/a}}{RT\rho_w}, \quad (5)$$

where $\sigma_{s/a}$ is the surface tension of the solution with respect to air, R is the universal gas constant, and T is the temperature. Although surface tension varies with temperature, the concentration of the solution [*Pruppacher and Klett*, 1997], and with the presence of surfactants [*Li et al.*, 1998], for simplicity we assume the value for pure water at 0°C (0.076 kg/s^2). With the assumptions of constant hygroscopicity and surface tension, equation (4) is a quartic polynomial (cubic when RH = 1) which can be solved analytically.

For RH between the crystallization and deliquescence RH of the aerosol, we compute the water content of each mode, assuming that particles are liquid, and compare this water content with that determined at the previous model time step. If the previous water content exceeds one half of the new water content, the particles are assumed to be wet as their past history (from the previous time step) suggests they are more likely wet than dry. If the previous water content is less than one half of the new water content, the particles are assumed to be dry. The approach attempts to account for the RH history of the particles, and the resulting temporally and/or spatially averaged water content versus RH has a smooth transition from between the crystallization and the deliquescence RH. We currently use a deliquescence RH of 80% and crystallization RH of 35% (appropriate for ammonium sulfate) for all aerosol modes and do not attempt to account for the complex behavior of the deliquescence of mixed aerosols.

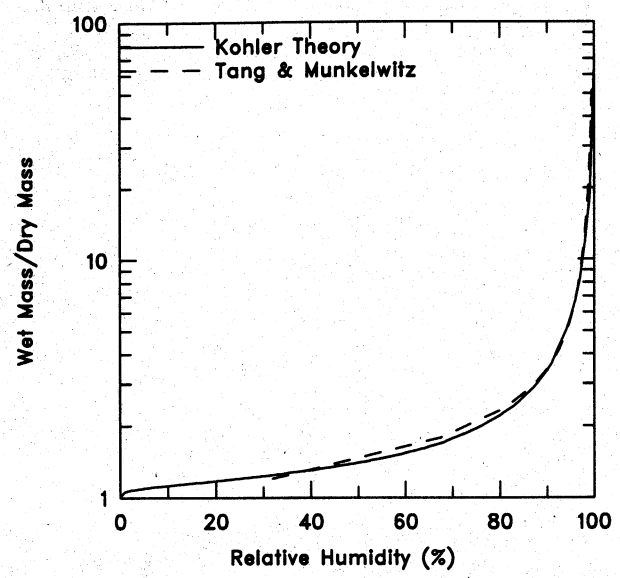

Figure 1. Ratio of wet mass to dry mass as a function of relative humidity for a 0.05 μm ammonium sulfate particle, according to Köhler theory and according to the parameterization of single-particle laboratory measurements of *Tang and Munkewitz* [1994].

Figure 1 compares the treatment of hygroscopic growth in MIRAGE with laboratory measurements [*Tang and Munkewitz*, 1994] for ammonium sulfate. The agreement is within 10% for relative humidity between 30 and 100%. Similar agreement is found for sodium chloride particles. This provides support for the MIRAGE treatment of hygroscopicity independent of solution strength. Laboratory measurements of hygroscopic growth are not available for organic aerosol particles or for mixtures of ammonium sulfate, sodium chloride, organic and black carbon, and soil dust. An evaluation of water uptake for real conditions would require measurements of the full composition of the aerosol [*McInnes et al.*, 1999; *Snider et al.*, 2000], which is beyond the scope of this paper. However, in section 3.2 we evaluate the influence of hygroscopic growth on aerosol extinction in a global aerosol simulation by MIRAGE.

Accurate simulation of aerosol water uptake obviously requires accurate values of aerosol composition and relative humidity. E2000 evaluate the MIRAGE simulation of aerosol composition. Figure 2 compares the zonal mean of the frequency that the column maximum relative humidity (RH_{max}) is less than 90%, as simulated by MIRAGE and as analyzed by ECMWF. The simulated RH_{max} exceeds 90% much more often than the ECMWF-analyzed RH_{max}, except at latitudes below 60°S. The simulated RH_{max} exceeds 99% 2-3 times more frequently than the ECMWF-analyzed RH_{max}, except in the Antarctic where the simulated relative humidity is usually lower than the analysis. These biases are probably due to the absence of a treatment of subgrid variability in stratiform cloud properties and microphysical processes in MIRAGE. Given the strong dependence of hygroscopic growth on relative humidity for relative humidity above 90%, the bias in the simulated relative humidity can be expected to produce excessively high aerosol optical depths in the vicinity of clouds. To permit a more meaningful comparison with ob-

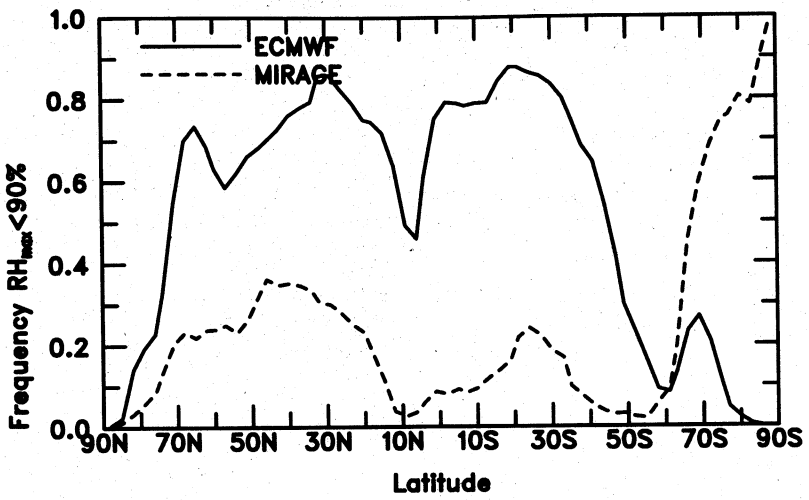

Figure 2. Zonal mean of the frequency that the column maximum relative humidity is less than 90%, as simulated by Model for Integrated Research on Atmospheric Global Exchange (MIRAGE) (dashed line) and as analyzed by ECMWF (solid line) for August 1994.

served aerosol extinction, we therefore have used the ECMWF-analyzed relative humidity to calculate water uptake in the simulations discussed here and in the companion papers (MIRAGE continues to predict clouds based upon its simulated relative humidity). Clearly further work to reduce this bias is needed before MIRAGE can be used in simulations without analyzed relative humidity.

3.2. Aerosol Radiative Properties

Given the wet aerosol composition, concentration, and size distribution, MIRAGE then uses a parameterization of the Mie theory for spherical particles to estimate the aerosol extinction cross section, single-scattering albedo, and asymmetry factor for all 18 CCM2 solar wavelengths and for the 10 μm water vapor window in the infrared. Although appropriate for wet aerosols, the spherical approximation is known to introduce errors as large as 100% for dry particles [*Mishchenko et al.*, 1995].

The parameterizations are expressed in terms of the wet surface mode radius and the wet refractive index. The wet surface mode radius r_s is related to the mean wet radius for a lognormal size distribution according to

$$r_s = r_w \exp[0.5 \log^2(\sigma_g)], \tag{6}$$

where σ_g is the geometric mean standard deviation of the lognormal size distribution. The wet refractive index n_w is determined from the volume-weighted mean of the refractive indices of water and each component of the dry aerosol:

$$n_w = \frac{1}{V_w} \sum_{j=0}^{J} \frac{n_j q_j}{\rho_j}, \tag{7}$$

where

$$V_w = \frac{4\pi N r_w^3}{3} \tag{8}$$

is the wet volume mixing ratio (m^3 g^{-1} air), and j=0 corresponds to water. The refractive indices of each of the aerosol species treated in GChM are listed in Table 1. Values for most species are from *Kent et al.* [1983], with the refractive index at 0.55 μm wavelength applied to all solar wavelengths and the value at 10.6 μm applied to the 10 μm water vapor window.

Given the wet radius and wet refractive index of a mode, the extinction coefficient (m^2 m^{-3} aerosol), σ_{ext}, single-scattering albedo ω and asymmetry factor g are parameterized as

$$\sigma_{ext} = \exp[\sum_{i=0}^{4} A_i T_i(x)], \tag{9}$$

$$\omega = \exp[\sum_{i=0}^{4} B_i T_i(x)], \tag{10}$$

$$g = \exp[\sum_{i=0}^{4} C_i T_i(x)], \tag{11}$$

where $x \equiv (2\log(r_s)-\log(r_{min})-\log(r_{max}))/(\log(r_{max})-\log(r_{min}))$, $T_i(x)$ is the Chebyshev polynomial of the order of i, and A_i, B_i, and C_i are coefficients interpolated bilinearly in complex wet refractive index from a table of coefficients for real and complex components of refractive indices spanning the range of refractive indices listed in Table 1. The table of coefficients are calculated at the beginning of each simulation by fitting Chebyshev polynomials to a set of Mie calculations of $\log(\sigma/(\rho_w V_w))$, $\log(\omega)$, and $\log(g)$ for lognormal size distributions spanning a range of surface mode radius from r_{min}=0.01 to r_{max}=10 μm. The fitting is done using the "chebft" numerical algorithm of *Press et al.* [1992]. The Mie calculations are performed for each of the 18 wavelengths treated in the CCM2 solar code and for the 10 μm window in the infrared. For wet surface mode radii larger than r_{max} the extinction coefficient is approximated by the geometric optics solution $\sigma_{ext}=1.5/r_s$.

The aerosol extinction optical depth for layer k follows from

$$\tau_k = \sigma_{ext} V_w \Delta M_k, \tag{12}$$

where ΔM_k is the mass per unit area of layer k.

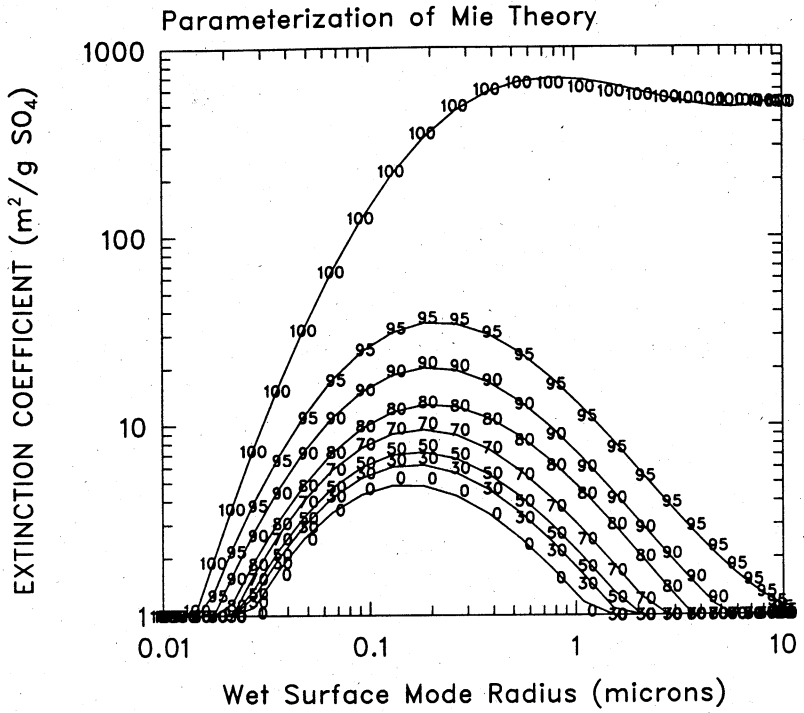

Figure 3. Extinction cross section of a lognormal distribution of ammonium sulfate particles as a function of wet surface mode radius and relative humidity, as parameterized in terms of wet surface mode radius and wet refractive index (solid lines) and as predicted by Mie theory for the same wet surface mode radius and wet refractive index (numbers denoting relative humidity). The numbers are centered at the Mie estimate. The geometric standard deviation of the size distribution is 2. The wavelength is 0.5 μm.

Figure 3 compares the extinction cross section calculated with the MIRAGE parameterization with that from Mie theory [*Wiscombe*, 1979] for a lognormal distribution of ammonium sulfate particles for a variety of relative humidities and wet surface mode radii. The agreement for the extinction cross section (which, of the three radiative properties of aerosol particles, is most sensitive to size and relative humidity) is excellent for wet surface mode radii between 0.01 and 10 μm and relative humidities between 0 and 100%. Of course, the Mie theory only applies to spherical particles, which is a good approximation for most aged particles but not for fresh primary particles such as dust and smoke, and the assumption of volume mixing is inappropriate for particles composed on an internal mixture of soluble and insoluble components [*Chylek et al.*, 1988, 1995]. Figure 3 is only an evaluation of the curve fitting to the Mie solution and should not be considered a full evaluation of the treatment of the aerosol optical properties in MIRAGE, which would require field measurements of aerosol composition and radiative properties [*Quinn et al.*, 1995].

The treatment of the combination of water uptake and aerosol radiative properties in MIRAGE is illustrated in Figure 4, which shows hourly samples of the ratio of the aerosol extinction cross section at a wavelength of 0.525 μm at ambient relative humidity at the surface to that for dry aerosols, plotted versus surface relative humidity for selected grid cells. This extinction ratio, which for a weakly absorbing aerosol is similar to the scattering ratio (also known as humidification factor) measured by humidigraph [*Charlson et al.*, 1984], is known to depend upon the aerosol composition, the relative humidity, and for some conditions also the history of relative humidity. The lowest extinction ratios are simulated over the Arabian Sea, where the extinction ratio is unity for all conditions because the aerosol is predominantly dust (E2000) and because the relative humidity is never high enough for deliquescence to occur. The highest extinction

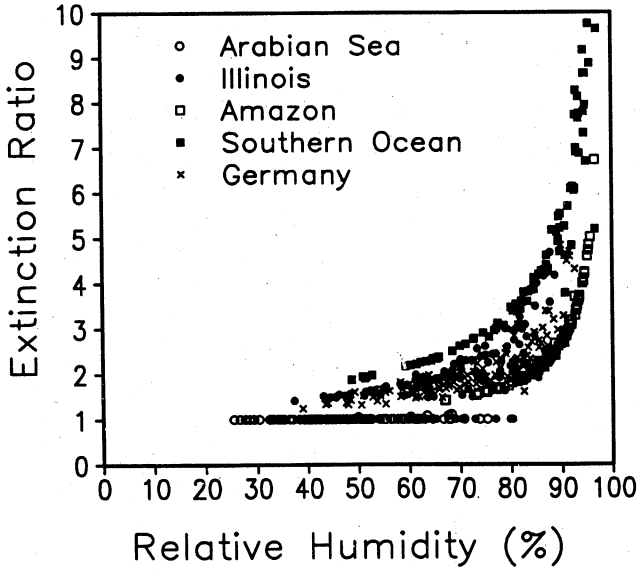

Figure 4. Ratio of aerosol extinction at ambient relative humidity to that for dry aerosol (at a wavelength of 0.525 μm) simulated at the surface every 6 hours during June 1994, plotted versus the surface relative humidity.

ratios at all relative humidities are in the Southern Ocean, which is dominated by the highly hygroscopic sea salt (E2000). Relatively low extinction ratios are simulated in the Amazon (which is dominated by weakly hygroscopic carbonaceous aerosol (E2000)), but the extinction ratio simulated at RH=80% (1.7) is still much higher than the mean value measured there by *Kotchenruther and Hobbs* [1999] (1.16). Somewhat higher extinction ratios are simulated in Germany, where the aerosol is composed of a mixture of carbonaceous and sulfate (E2000). The extinction ratio simulated off the east coast of the United States at RH=80% (not shown) is about 3, which is larger than values (1.5-2.5) measured from aircraft [*Kotchenruther et al.*, 1999], perhaps because the extinction ratio at the surface is influenced by the more hygroscopic sea salt. The extinction ratio at RH=80% measured on Sable Island by *McInnes et al.* [1998] is consistent with the MIRAGE simulation for a marine air mass but is much smaller (about 1.6) for a polluted air mass. Perhaps the most interesting distribution of extinction ratio is simulated in Illinois, where sulfate is the dominant aerosol (E2000) and hysteresis is clearly evident for relative humidity between 40 and 80%.

3.3. Aerosol Optical Depth

MIRAGE simulates a mixture of aerosol that varies in space and time with emissions and with the simulated meteorology. The variations in the aerosol concentration, size distribution, and composition produce variations in the aerosol optical depth, single-scattering albedo, and radiative forcing.

To evaluate the simulation of aerosol optical depth, we compare the MIRAGE simulation with estimates from both surface and satellite measurements. The advantage of surface measurements is high accuracy, while the advantage of satellite measurements is near-global coverage. Appendix A describes the surface data set.

In comparing simulated and observed optical depths it is essential to ensure that averages are formed for the same conditions. This is illustrated in Figure 5, which compares the seasonal cycle of monthly mean simulated and observed aerosol optical depth at a wavelength of 500 nm for Albany New York. The observed optical depth can only be estimated when the Sun is not obscured by clouds. The simulated optical depth is calculated every hour and hence can be averaged under cloudy as well as clear conditions. Since one might expect the simulated aerosol optical depths to vary with relative humidity and cloudiness, it is important to filter the simulated optical depth in a manner consistent with the implicit filtering of the observed optical depth. To test the impact of filtering on the monthly mean simulated optical depth, Figure 5 shows the simulated monthly mean aerosol optical depth with no filtering and with filtering by the availability of observed optical depths, and with filtering by the cloud optical depth, the column maximum relative humidity and the availability of observed optical depths. The cloud optical depth filter is applied when the simulated cloud optical depth exceeds 1.0. The column maximum relative humidity filter is applied when the ECMWF-analyzed column maximum relative humidity exceeds 99% (although subgrid variations in relative humidity should be quite important, if the grid cell mean relative humidity is 99% [*Haywood et al.*, 1997; *Ghan and Easter*, 1998], they are neglected in MIRAGE). As might be expected, the filtering reduces the monthly mean simulated optical depth considerably, with reductions of 15-50%. Almost all of the reduction is due to filtering according to the availability of observations, with very little sensitivity of the simulated optical depth to the cloud optical depth and column maximum relative humidity filter after the observational availability filter has been applied. Such a result indicates that the relative humidity used to calculate water uptake in MIRAGE (the ECMWF-analyzed relative humidity) is highly correlated with the con-

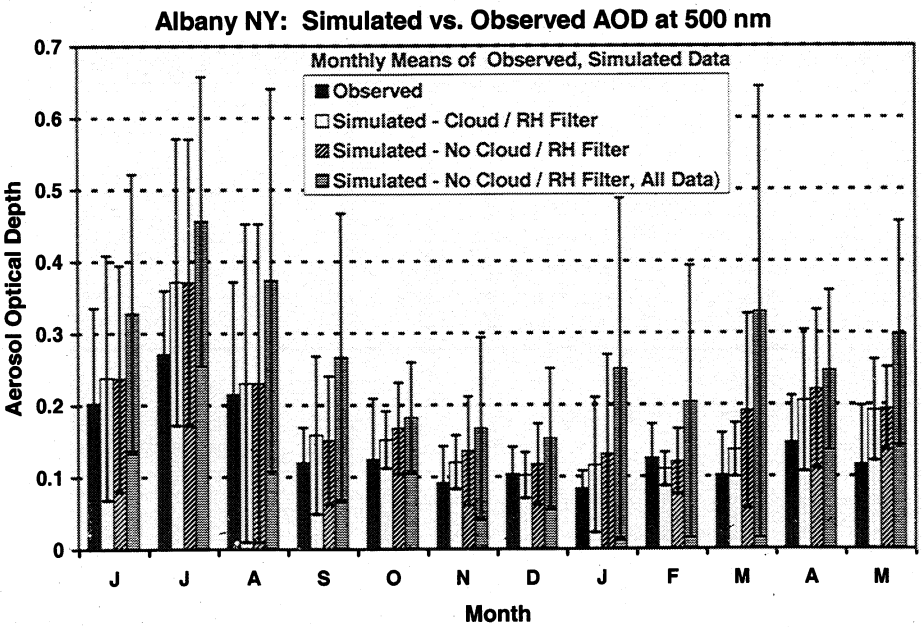

Figure 5. Monthly mean aerosol optical depth (500 nm wavelength) as observed at Albany New York and as simulated by MIRAGE at the nearest grid point, filtered by the availability of observations (no cloud/RH filter), filtered by the availability of observations and by the column maximum relative humidity (cloud/RH filter), and unfiltered (all data).

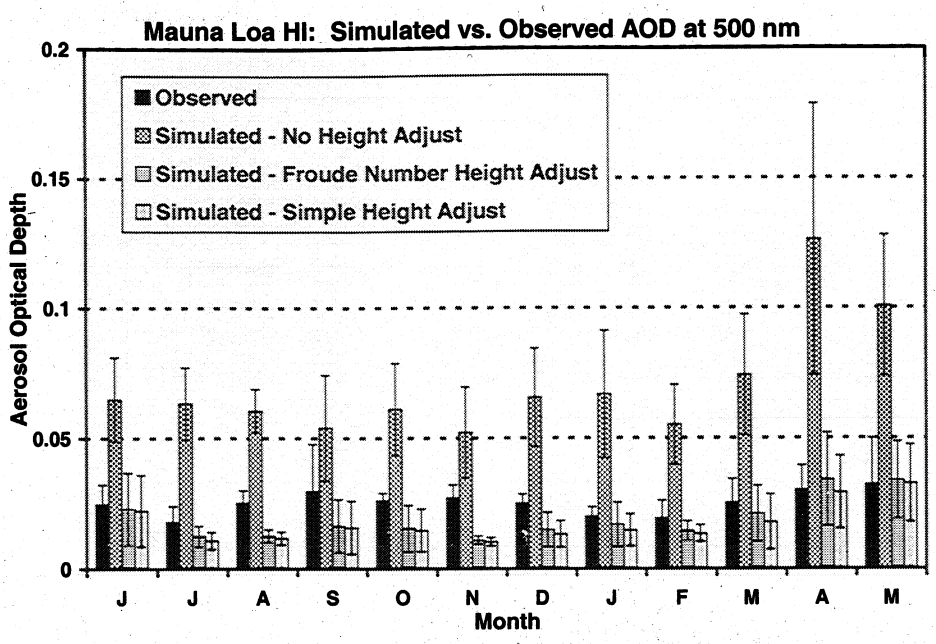

Figure 6. Monthly mean aerosol optical depth as observed at Mauna Loa and as simulated by MIRAGE at the nearest grid cell with no height adjustment, with a simple adjustment for the difference in the heights of the measurements and the model grid cell, and with Froude-number-dependent adjustment.

ditions (i.e., clouds) that prevent aerosol optical depth estimates from the measured radiance (it is unlikely that this result would apply in a model that did not use an observationally constrained relative humidity to estimate water uptake). In comparison with the observed optical depth, the simulated optical depth with filtering agrees much better than the unfiltered optical depth. The summertime maximum in optical depth is simulated correctly by MIRAGE.

Further adjustments in the simulated optical depth are required for grid points with surface elevation differing significantly from that of the corresponding surface station. Figure 6 compares the column aerosol optical depth simulated by MIRAGE at the grid point closest to Mauna Loa with that estimated from surface measurements at Mauna Loa. The simulated total column optical depth is much larger than observed because the Mauna Loa measurements are taken at an altitude of 3400 m, far above the surface elevation of the MIRAGE grid point closest to Mauna Loa. The simulated total column optical depth includes contributions from elevations far below the Mauna Loa observatory. A direct comparison between the simulated and the observed optical depth must account for the difference in the surface elevation of the measurements and the model, and the influence of the elevation difference on the optical depth. As a first correction, we have subtracted from the simulated optical depth the contribution from elevations below the elevation of Mauna Loa. The agreement between simulated and observed optical depth, also shown in Figure 6, is much better than without the correction. However, such a correction is likely to overestimate the influence of surface elevation on column optical depth because air does not always flow around mountains. For sufficiently strong winds air can flow over mountains, carrying with it the pollutants from lower elevations. Indeed, the optical depths using this first correction are lower than observed. As a second correction, we have used the Froude number parameterization of *Leung and Ghan* [1998] to estimate the dividing streamline height (DSH) for elevated sites. Air above the DSH is able to pass over a topographical barrier having the same elevation as the site, while air below the DSH must move around the barrier. The Froude number corrected aerosol optical depth is that of the air mass above this DSH. As expected, the optical depths with the Froude number correction are higher than without it and are in better agreement with the observations. All subsequent comparisons with surface station measurements of aerosol optical depth therefore use the Froude number correction to the simulated aerosol optical depth.

Figure 7 summarizes the comparison between the station measurements of aerosol optical depth and the MIRAGE simulation. Each point plotted represents a monthly mean (if available) for one of the 56 stations. Monthly means are formed only for times when both MIRAGE and the measurements were cloud free. Although MIRAGE clearly demonstrates skill in simulating optical depth, aerosol optical depth is underestimated by up to 0.9 for some stations and months. These large differences occur primarily at stations in Brazil during the biomass burning season, stations in central Canada during the wildfire season, and stations in Asia and off the west coast of Africa which are strongly influenced by soil dust. One the other hand, MIRAGE overestimates aerosol optical depth for some stations in Europe and North America by 100% or more.

In most regions these errors are most likely due to errors in the simulated concentrations of the aerosol. E2000 find that MIRAGE underestimates organic carbon at most locations where and when biomass is burned (where simulated aerosol optical depths are low) and also find that MIRAGE underestimates dust concentrations downwind of the major dust production regions in Africa and Asia (where simulated optical depths are also low). Over Europe and North America, where MIRAGE overestimates aerosol optical depth, E2000 find that MIRAGE simulates excessive sulfate above the planetary boundary layer.

The evaluation of the simulated aerosol optical depth can be extended to global scales by comparing with satellite estimates. Figure 8 compares the August 1994 mean aerosol

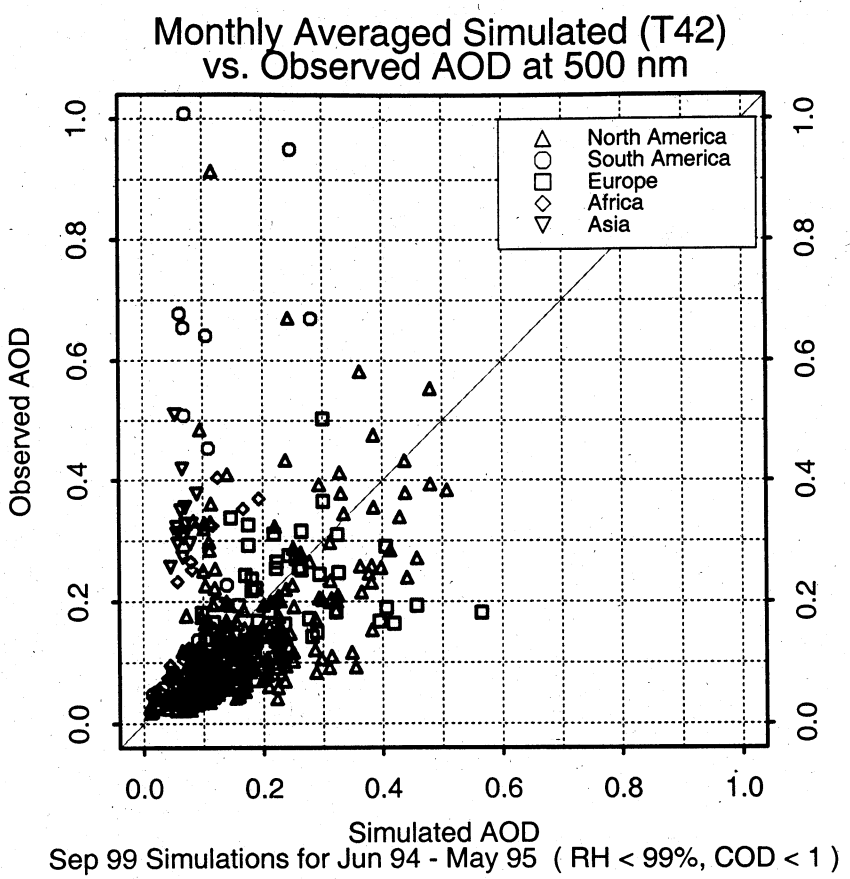

Figure 7. Scatterplot of the observed monthly mean aerosol optical depth for each month and station plotted versus the monthly mean aerosol optical depth simulated by MIRAGE. Averages have been formed only for times when both the simulations and the observations are available and the MIRAGE column maximum relative humidity is less than 99%.

optical depth as simulated by MIRAGE and as estimated from AVHRR radiance measurements using the methods of *Wagener et al.* [1997] and *Stowe et al.* [1997]. The domain has been restricted to latitudes 10°S-80°N because the satellite orbit did not permit daytime measurements in the Southern Hemisphere. To eliminate differences associated with differences in the timing of samples, the monthly means have been formed from samples when the aerosol optical depth can be determined from measurements, i.e., when the ocean surface can be observed in daylight. For the Wagener et al. estimates the observations are averaged over all AVHRR pixels within each T42 grid cell. The simulated values are also filtered by times when the column maximum relative humidity exceeds 99%. By filtering out cloudy conditions the periods of greatest water uptake are eliminated. MIRAGE captures many of the qualitative features of the spatial distribution, including the plumes moving eastward from the continental United States and China and moving westward from West Africa, the high optical depth in the Mediterranean and Arabian Seas, and low optical depth near Bermuda. However, quantitatively, the simulated and observed aerosol optical depths can be quite different. MIRAGE evidently simulates too much aerosol off the east coasts of the United States and Asia and too little dust off the coast of West Africa and in the Arabian Sea. Most obvious perhaps is the excessive aerosol in remote regions, particularly the equatorial Pacific, Atlantic, and Indian Oceans. Many of the features of the Wagener et al. analysis are also evident in the NOAA [*Stowe et al.*, 1997] analysis. Given the differences in the two methods for estimating aerosol optical depth from radiance measurements, the consistency of most of the simulation biases identified by comparison with the NOAA and Wagener et al. analyses are likely to be real rather than artifacts of errors in the analyses.

However, it must be recognized that there is uncertainty in the estimate of the aerosol optical depth from the measured radiance. Figure 9 shows a scatterplot of the aerosol optical depth as simulated and as estimated from AVHRR measurements by the Wagener et al. algorithm for all grid cells. Although no systematic bias is evident, the large negative values of the observed optical depth indicate the magnitude of the uncertainty in the observations. Such an uncertainty is to be expected given that the observations are estimated from the difference between the radiance measured by the satellite and an estimate of what the measured radiance would be in the absence of aerosol. Small errors in the estimate of the surface reflectance can introduce substantial errors in the estimated aerosol optical depth. The widespread low values of observed aerosol optical depth across the tropical oceans are associated with the negative values in the scatterplot and hence do not indicate excessive simulated optical depths there. The uncertainty is greatest in the tropics because the solar zenith angle was highest there for the sun-synchronous orbit of the NOAA 11 satellite during August 1994.

3.4. Aerosol Single-Scattering Albedo

All estimates of aerosol optical depth from satellite radiance measurements must assume characteristic compositions and size distributions for the aerosol. To test the

universality of such assumptions, Figure 10 shows the spatial distribution of the mean 0.525 μm wavelength single-scattering albedo (SSA) of the dry aerosol in the lowest layer simulated by MIRAGE for June 1994 to May 1995. The time mean is formed by weighting by the dry aerosol extinction. By focusing on the SSA for the dry aerosol, the influence of water uptake on the single-single scattering albedo is eliminated. This permits comparison with surface measurements that are typically under dry conditions for the same reason. Considerable spatial variability is evident, with mean simulated SSA exceeding 0.96 over almost all of the oceans and values less than 0.7 in Madagascar and central and South Africa where the column burden of black carbon is as much as 40% of the total dry aerosol. The biomass burning region of central Africa produces values less than 0.8 across all of central Africa. Values are between 0.9 and 0.96 for most of the continental United States but with values as low as 0.66 in the southwest and 0.80 in the northeast. In most of Europe the mean simulated SSA is less than 0.9 with values as low as 0.72, due to high black carbon emissions associated with combustion of coal and diesel fuel (see E2000). The mean SSA in Brazil, where biomass burning is common, is 0.87-0.93, and in Bolivia the mean SSA is as low as 0.8. The mean SSA over China is not so low as might be expected on the basis of its reliance on coal for energy production.

At higher levels in the troposphere the distribution of single-scatter albedo (not shown) exhibits the characteristics of horizontal transport by the prevailing winds. A strong

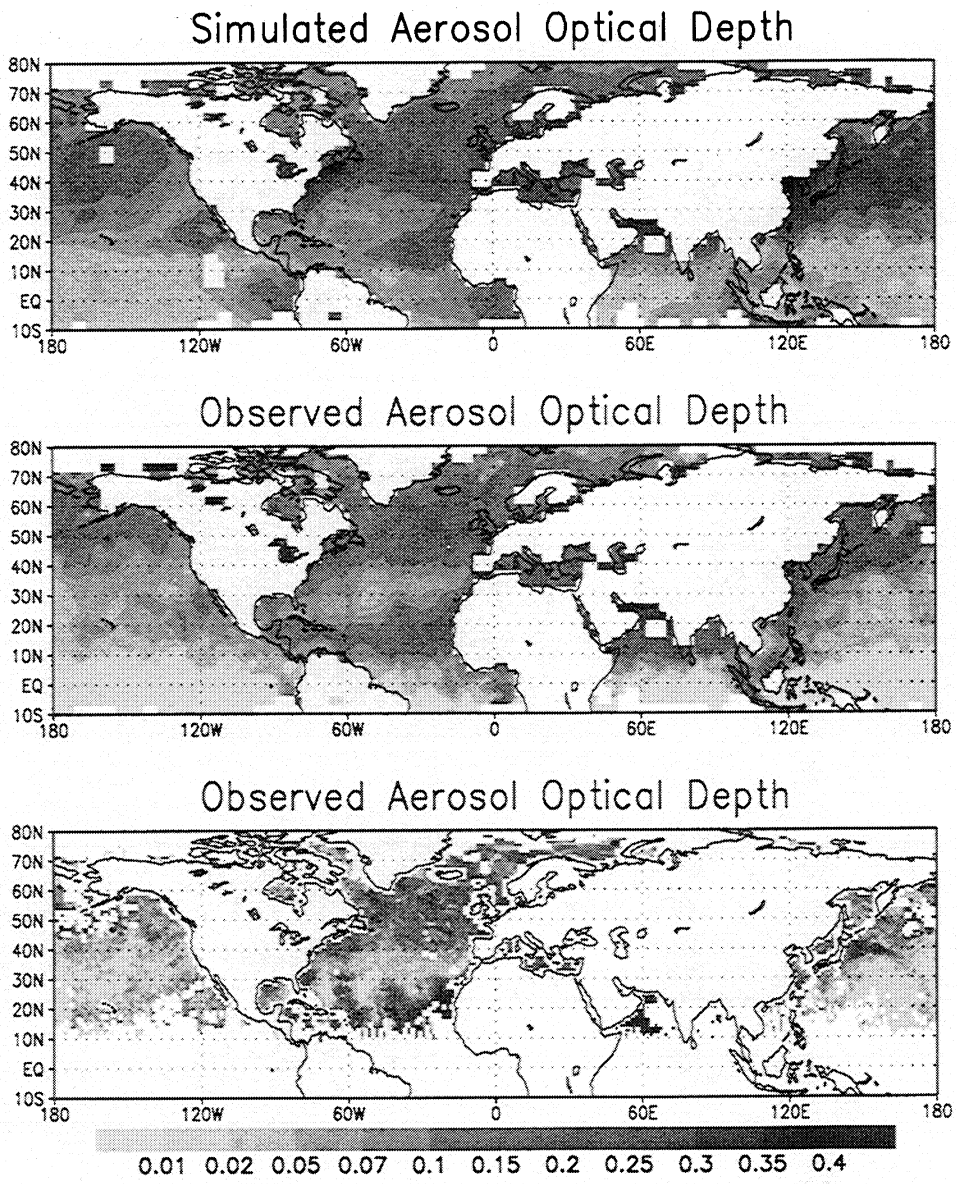

Figure 8. August 1994 mean spatial distribution of the aerosol optical depth as simulated by MIRAGE (top), as estimated from AVHRR radiance measurements using the *Wagener et al.* [1997] algorithm (middle), and as estimated by the NOAA [*Stowe et al.*, 1997] algorithm (bottom). The simulated optical depth has been averaged over all times that the observed optical depth can be determined using the Wagener et al. algorithm, excluding times when the column maximum relative humidity exceeds 99%. The Wagener et al. estimates have been averaged over all pixels with each T42 grid cell. Observations are not possible over land, at twilight or night, or under cloudy conditions.

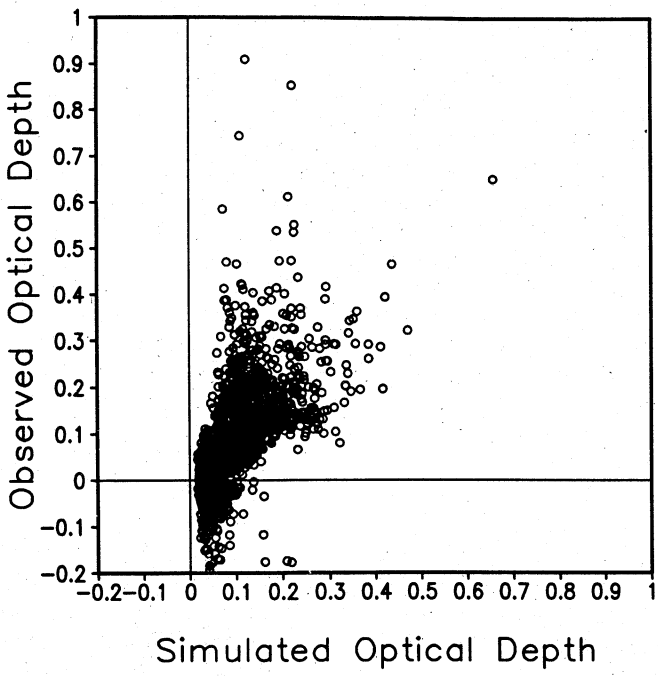

Figure 9. Scatterplot of the simulated versus observed [*Wagener et al.*, 1997] aerosol optical depths (August 1994 averages) illustrated in Figure 7.

plume of low single-scatter albedo is simulated eastward from South Africa to Australia.

The low values of simulated single-scattering albedo largely reflect the fractional concentration of black carbon, which is the only aerosol component that absorbs visible radiation. Although both the real and the imaginary components of the refractive index for black carbon (Table 1) are larger than those used in other modeling studies [*Haywood and Shine*, 1995; *Schult et al.*, 1997], the radiative properties of pure black carbon are insensitive to the difference in the refractive index. However, the radiative properties of a dilute internal mixture of black carbon and other components are sensitive to the value of the refractive index for black carbon. The plume of low SSA downwind of South Africa is therefore sensitive to the value of the refractive index of black carbon; a lower value for the imaginary component would yield significantly higher values of the SSA.

Both satellite and in situ measurements are available for evaluating the simulated single-scattering albedo. Nimbus 7 Total Ozone Mapping Spectrometer (TOMS) measurements provide global information about the frequency of UV-absorbing aerosols above the boundary layer [*Herman et al.*, 1997a], but aerosols in the boundary layer cannot be detected and the frequency of UV-absorbing aerosols does not always translate into a time mean single-scatter albedo at visible wavelengths. Moreover, the TOMS analysis is not available

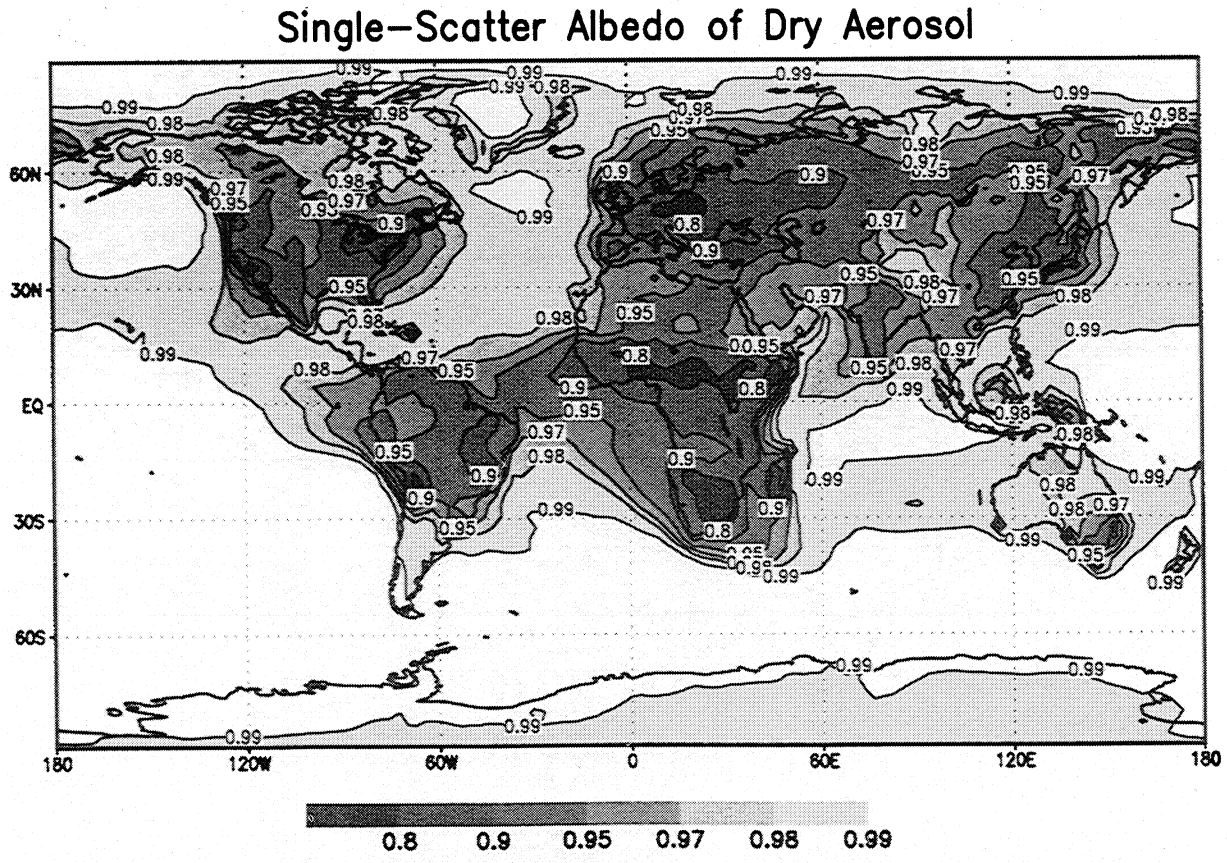

Figure 10. Spatial distribution of the surface air dry aerosol single-scattering albedo simulated by MIRAGE for June 1994 to May 1995. The monthly mean is formed by weighting by the dry aerosol extinction.

for the period of the MIRAGE simulation. However, the low SSA simulated in sub-Saharan Africa is at least qualitatively consistent with the high frequency of UV-absorbing aerosols detected there by the TOMS analysis [*Herman et al.*, 1997a].

In situ measurements provide quantitative estimates of single-scattering albedo that can be compared with the MIRAGE simulation. Table 2 compares the simulated single-scattering albedo at the surface with in situ measurements. The simulated single-scattering albedo has been averaged for the same time of year as the measurements. All in situ measurements are at the surface except for the aircraft measurements of *Hegg et al.* [1998] and *Reid et al.* [1998]. Note that *Bond et al.* [1999] have identified errors in the absorption photometer response to light scattering, and *Anderson and Ogren* [1998] have found that angular nonidealities in the nephelometer can cause particle scattering in the near-forward direction to be underestimated. Only the measurements at Cheeka Peak have been corrected for these errors, which tend to produce estimates of the SSA which are too low by 0.05 to 0.10. Although it might be tempting to attribute the excessively high values of SSA simulated by MIRAGE at Kamchatka, Wellington, Allegheny Mountains, and the tropical Atlantic to measurement bias, the simulated SSA is much lower than observed at Bondville and Abastumani. The excessively low simulated SSA could be attributed to the value of the refractive index of soot, which is higher in the MIRAGE simulation than the value used by other investigators. The excessively high SSA in the tropical Atlantic could be due to poor emissions of soot from central Africa, but the SSA simulated by *Liousse et al.* [1996] using the same soot emissions is much closer to the measurements, albeit still much higher (it should be noted that *Liousse et al.* compare the simulated column mean rather than surface SSA with surface measurements). The SSA bias at Allegheny Mountains might be much smaller than it appears to be, because measurements at nearby Shenandoah are much closer to the simulated SSA there than to SSA measured at Allegheny Mountains.

Single-scattering albedo also varies in time as well as space. Figure 11 compares the frequency distributions of hourly dry SSA at Cheeka Peak (near the Pacific coast in Washington State) as simulated for March and April 1995 by MIRAGE and as measured during March and April 1997 by *Anderson et al.* [1999]. Although the medians of the frequency distributions are similar, the observed frequency distribution is bimodal, while the simulated distribution is

Table 2. Simulated and Observed Aerosol Single-Scatter Albedo

Location	Period	Observed	Simulated
Arctic (82.5°N, 62.5°W)	annual	0.96[a]	0.97
Ny Alesund (79°N, 12°E)	annual	0.95[a]	0.99
Spitsbergen (79°N, 12°W)	annual	0.93-0.97[b]	0.98
Barrow (71.2°N, 156.3°W)	annual	0.96[c]	0.98
Stockholm (59.2°N, 18°E)	annual	0.89[a]	0.86
Kamchatka (56°N, 160°E)	May	0.88[d]	0.99
Cheeka Peak (48.3°N, 124.6°W)	March	0.85-0.97[e]	0.87
Sable Island (43.9°N, 60.0°W)	annual	0.86-0.97[f]	0.97
Abastumani (41.4°N, 42.5°E)	July	0.89[g]	0.80
Bondville (40.1°N, 88.4°W)	annual	0.86-0.97[f]	0.84
Alleghenny Mountains (38.3°N, 80°W)	Aug.	0.87[h]	0.98
Shenandoah (38°N, 78°W)	July	0.95[i]	0.98
TARFOX (37.5°N,74°W)	Aug.	0.90[j]	0.94
Mesa Verde (37.1°N, 108.3°W)	Sept.	0.91[g]	0.93
Sagres (37°N,9°W)	July	0.94[k]	0.94
Oklahoma (36.6°N, 97.5°W)	annual	0.92-0.99[f]	0.96
Anderson Mesa (35.1°N, 111.4°W)	Nov.	0.94[g]	0.95
Mauna Loa (19.3°N, 155.4°W)	annual	0.97[c]	0.99
Kaashidhoo (5.0°N, 73.5°E)	Feb.	0.87-0.90[l]	0.96
Tropical Atlantic (5°S, 20°W)	Aug.	0.8[d]	0.98
Cuiabá (16°S,56°W)	Aug.	0.85[m]	0.89
West Australia (34.2°S, 115.1°E)	June	0.998[d]	0.98
Wellington (41.2°S, 174.5°E)	June	0.88[d]	0.98
South Pole (89°S, 102°W)	annual	0.97[c]	0.98

[a] *Heintzenberg* [1982].
[b] *Heintzenberg and Leck* [1994].
[c] *Bodhaine* [1995].
[d] *Clarke* [1989].
[e] *Anderson et al.* [1999].
[f] *Ogren et al.* [1999].
[g] *Waggoner et al.* [1996].
[h] *Japar et al.* [1986].
[i] *Ferman et al.* [1981].
[j] *Hegg et al.* [1997].
[k] *Carrico et al.* [2000].
[l] *Satheesh and Ramanathan* [2000].
[m] *Reid et al.* [1998].

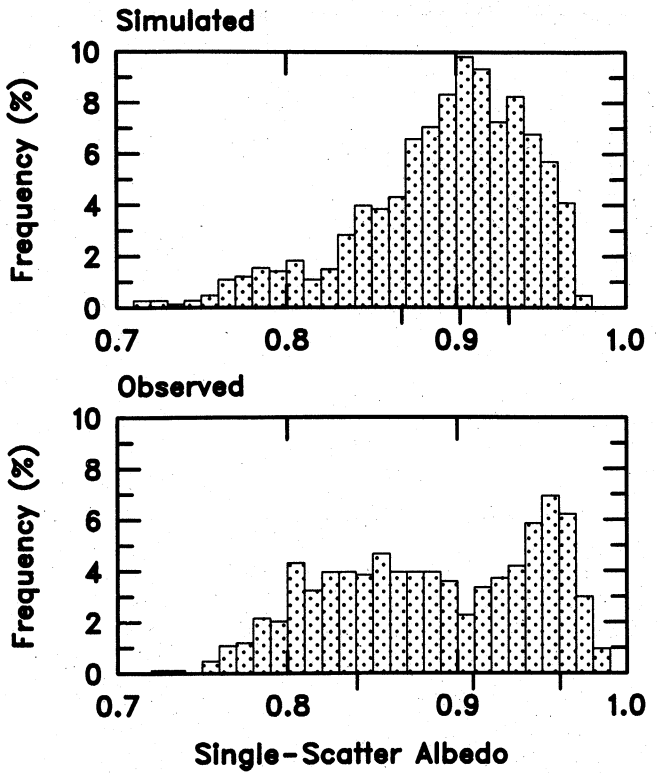

Figure 11. Frequency distributions of hourly single-scattering albedo of dry aerosol at Cheeka Peak for March and April, as simulated by MIRAGE for 1995 and as measured by *Anderson et al.* [1999].

dominated by one mode with only a small secondary mode. Clearly reporting the full frequency distribution of measured single-scattering albedo (or at least a variety of percentile values) would be of much greater value than the common practice of reporting only a single mean value.

3.5. Ångström Exponent

Information about the aerosol size distribution is expressed by the Ångström exponent, which depends on the ratio of aerosol optical depth at two reference wavelengths [*King et al.*, 1999]. Figure 12 shows the spatial distribution annual mean Ångström exponent as simulated by MIRAGE. Both the MIRAGE simulation and the estimates from POLDER satellite measurements [*Deuze et al.*, 1999] and SeaWiFS satellite measurements [*Wang et al.*, 2000] show high values along the coastlines of central America, the eastern United States, western South America, the Mediterranean Sea, sub-Saharan and central Africa, Madagascar, India, Indonesia, China, and Japan. These high values reflect the emissions of submicron primary particles and secondary aerosol precursor gases from the adjacent continents, a feature that is clearly evident in the MIRAGE simulation. Much lower values of the Ångström coefficient simulated by MIRAGE are evident across and downwind from Saharan Africa, Arabia, the Tibetan Plateau, Australia, and Patagonia, and in the storm track between latitudes 50° and 60°S. These low values reflect the emissions of coarse mode dust and sea-salt particles in these regions. Comparing with the POLDER and SeaWiFS estimates, the MIRAGE estimate is a factor of 2-4 higher than both satellite estimates over most of the ocean

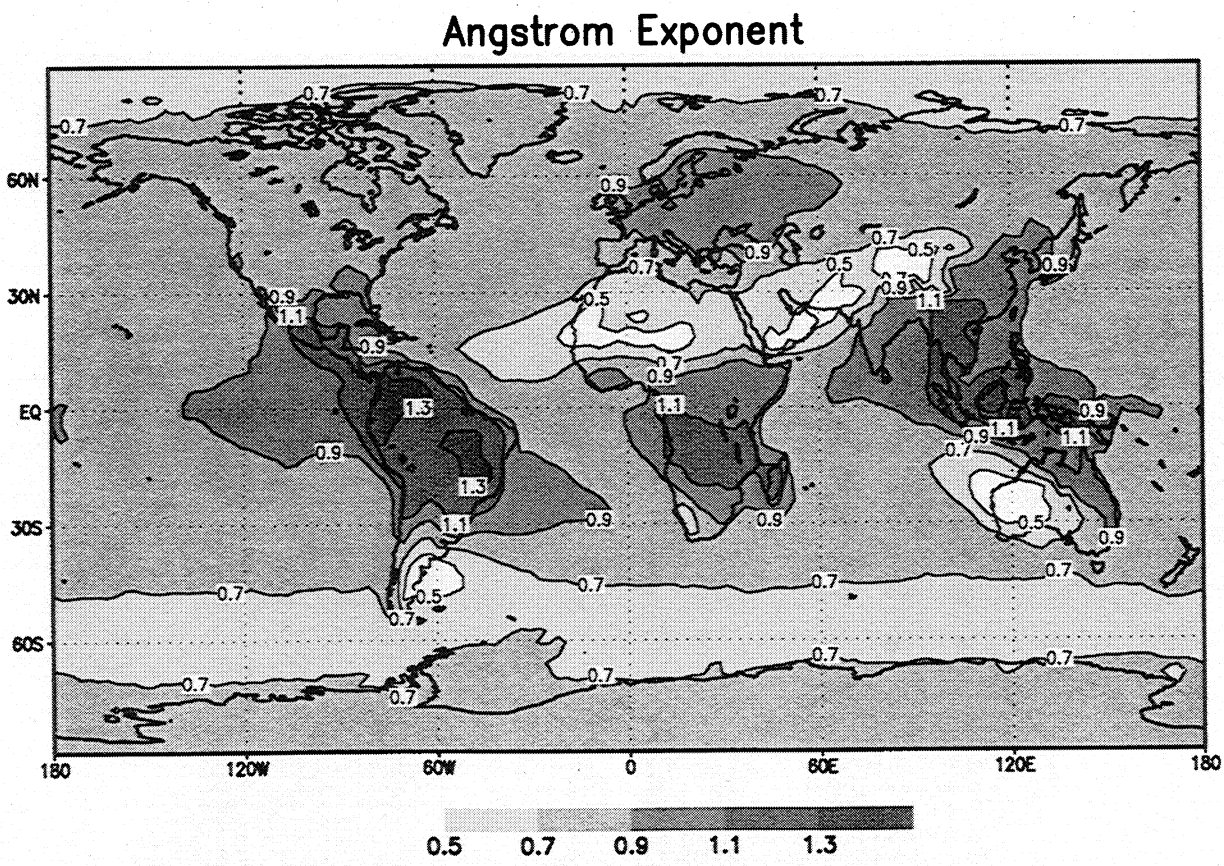

Figure 12. Ångström exponent simulated by MIRAGE for June 1994 to May 1995, averaging only when the column maximum relative humidity is less than 95%.

(satellite estimates are not yet available over land). This bias cannot be attributed to the fact that the POLDER and SeaWiFS estimates are based on wavelength ranges 0.670-0.865 μm and 0.765-0.865 μm, respectively, while the MIRAGE estimate is based on wavelength range 0.3275-0.525 μm; the MIRAGE estimate of the Ångström coefficient for the wavelength range 0.525-2.85 μm is in all regions larger than the estimate for visible wavelengths, so the estimate for wavelengths 0.3275-0.525 μm is lower than it would be for the POLDER and SeaWiFS wavelengths. Part of the explanation for the MIRAGE overestimate of the Ångström coefficient is a bias in the satellite estimates; the estimate from POLDER measurements is known to be about 30% too high at optical depths greater than 0.1 [*Goloub et al.*, 1999] but may be larger than 30% at optical depths near 0.1 (which are common across most of the ocean). Indeed, estimates from OCTS satellite measurements [*Nakajima and Higurashi*, 1998] and from surface AERONET measurements (S. Kinne, personal communication, 2000) are much closer to the MIRAGE simulation over the remote oceans. Of course, part of the overestimate could also be due to a bias in the size distribution simulated by MIRAGE; further comparison with surface estimates of the Ångström coefficient at marine sites will be needed to isolate this bias.

3.6. Sensitivity of Aerosol Radiative Forcing to Aerosol Optical Depth

Further evidence that the aerosol composition and size distribution are not universal can be seen in the distribution of the sensitivity of the aerosol radiative forcing to aerosol optical depth, which is typically estimated from $\Delta F/\tau$ where ΔF is the difference between the top-of-the-atmosphere radiative flux with and without aerosol. For aerosol optical depths much less than 1 the radiative forcing sensitivity is independent of the aerosol optical depth and depends largely on the aerosol single-scatter albedo, the surface albedo, and on the solar zenith angle. The radiative forcing sensitivity is illustrated in Plate 1 for June 1994 to May 1995 of the MIRAGE simulation, averaged over times when the column maximum relative humidity is less than 70%. Consistent with the estimates of *Ogren et al.* [1999], *Russell et al.* [1999], and *Anderson et al.* [1999] from measurements, the radiative forcing sensitivity is typically -20 to -40 W m^{-2} over much of the Northern Hemisphere, with the exception of Greenland and the Arctic ice where the surface albedo is high enough to change the sign of the forcing. Consistent with the distribution of single-scatter albedo the radiative forcing sensitivity is much smaller over Europe and even changes sign over South Africa, where the single-scattering albedo is particularly low. The radiative forcing sensitivity is most negative (down to -70 W m^{-2}) over the tropical oceans, where the insolation is greatest and the surface albedo is lowest. The radiative forcing sensitivity is much smaller (-10 to +10 W m^{-2}) across the high latitude oceans of both hemispheres, reflecting both the weaker insolation and the higher surface albedo at high solar zenith angles there, and over Saharan Africa, where the surface albedo is relatively high. The radiative forcing sensitivity is generally more negative over the Pacific Ocean than over the Atlantic Ocean, reflecting the slightly higher single-scattering albedo over the Pacific Ocean. Clearly, more measurements of the spatial distribution of the radiative forcing sensitivity are needed to determine where the radiative forcing sensitivity to aerosol optical depth simulated by MIRAGE is realistic in other regions.

Further evidence of variability in aerosol size distribution and composition is illustrated in Figure 13, which shows the zonal and annual mean contributions of each of the four aerosol modes to the total aerosol optical depth. The accumulation mode dominates at all latitudes except in the Southern Hemisphere storm track (50°-70°S latitude), where the sea-salt mode dominates. The dust mode produces a mean optical depth of 0.03 at latitudes 15°-40°N and 0.01 at latitudes 20°-30°S. The Aitken mode produces negligible optical depths because of the small size of the particles. The high aerosol optical depth in the Arctic is associated with the high frequency of ECMWF column maximum relative humidity exceeding 90% (Figure 2); the radiative forcing associated with the Arctic aerosol is relatively weak because it occurs predominantly during the Arctic winter, when insolation is low or zero. The contributions of the components to the global and annual mean column mass loading of each mode are summarized in Table 3. Aerosol water dominates the column mass loading for the sea-salt mode and to a lesser

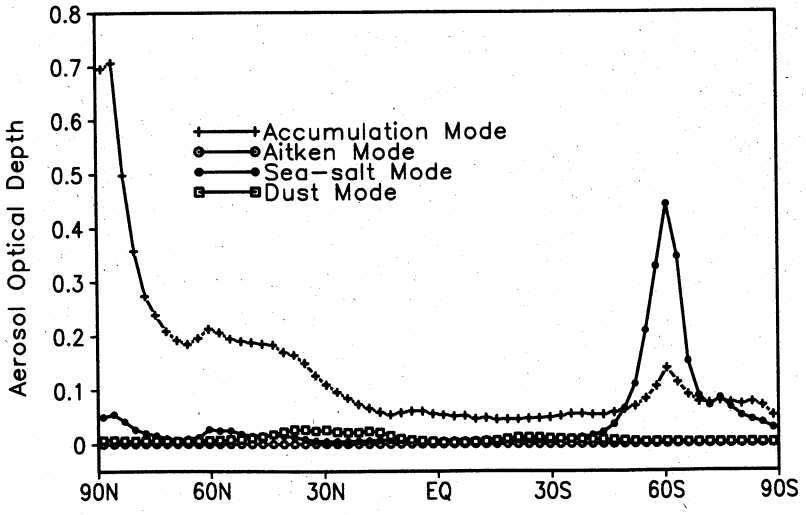

Figure 13. Zonal and annual mean aerosol optical depth simulated by MIRAGE for the accumulation, Aitken, dust, and sea-salt modes.

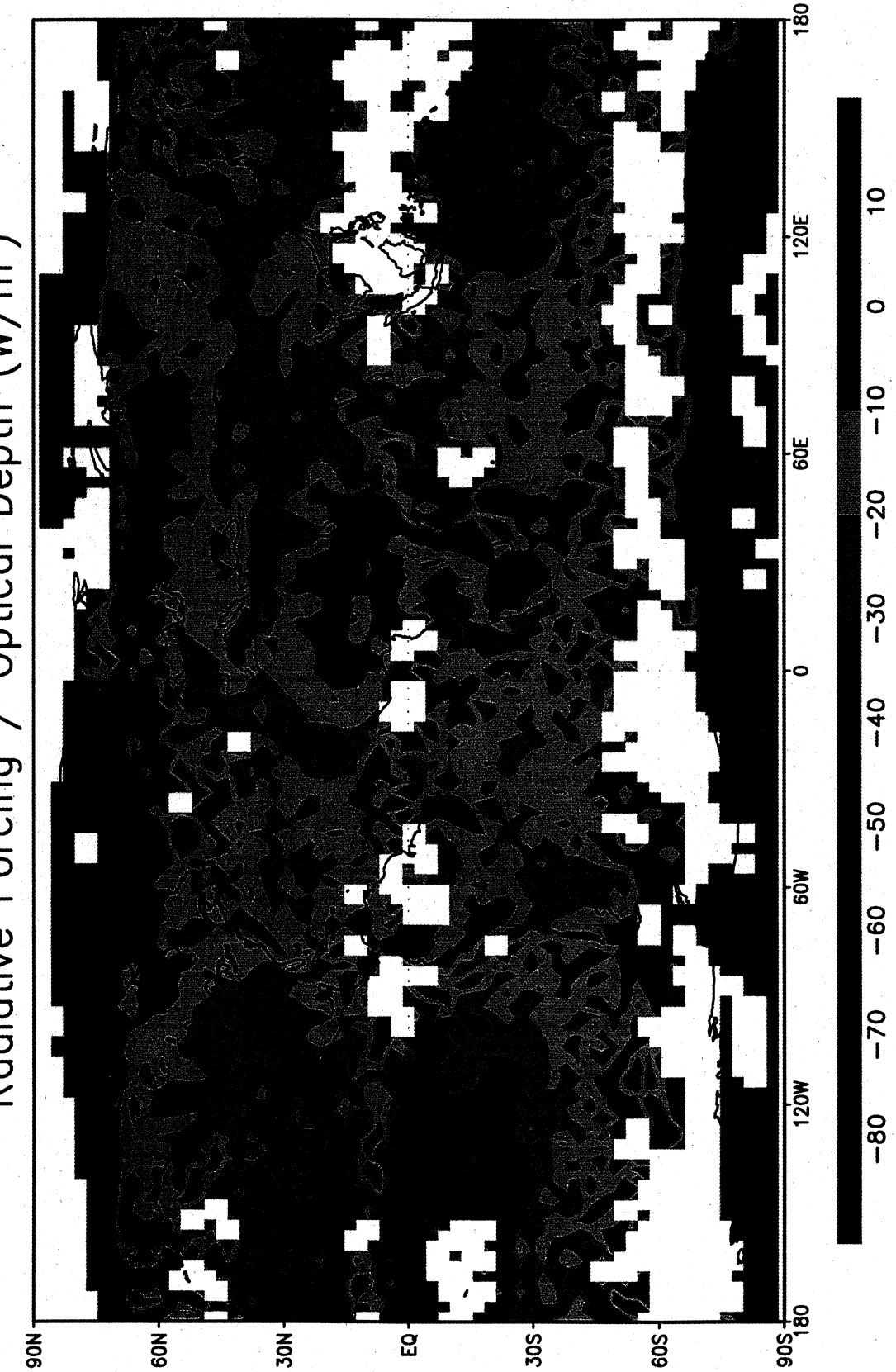

Plate 1. Radiative forcing per unit optical depth simulated by MIRAGE for June 1994 to May 1995. Times when the column maximum relative humidity exceeds 70% have been filtered from the temporal averaging.

Table 3. Column Mass Loading (mg m^{-2}) for Each Mode

	Accumulation	Sea Salt	Dust
Water	15.4	2018	2.0
Sulfate	8.8	0.00	0.1
MSA	0.2	0.000	
Organic carbon	2.7		
Black carbon	0.4		
Soil dust	0.2		8.4
Sea salt	0.2	8.4	

extent the accumulation mode, particularly in the Southern Hemisphere storm track, but only contributes 20% of the dust mode. The contribution of water to the optical depth of the sea-salt mode is probably overestimated for two reasons: (a) the treatment is based upon the Köhler equilibrium theory, which neglects kinetic effects and hence overestimates the response to high relative humidity for coarse particles, and (b) the ECMWF relative humidity can be near or at 100% at times when MIRAGE does not simulate clouds, so that none of the particles are activated and hence all can take on water and contribute to the aerosol optical depth. After water, sulfate comprises the largest fraction of the accumulation mode, followed by organic carbon and then black carbon. The substantial contribution of organic carbon to the aerosol optical depth is consistent with measurements in the Tropospheric Aerosol Radiative Forcing Observational Experiment [*Hegg et al.*, 1997]. Sulfate contributes little to the sea-salt mode and only 1% of the dust mode. Most of the spatial variability of the optical depth of the accumulation mode and the sea-salt mode is due to variability in the aerosol water loading. Figure 14 shows this for the accumulation mode: the aerosol water loading is greatest at those latitudes (90°N and 60°S) with the highest frequency of relative humidity higher that 90% (Figure 2).

3.7. Aerosol Radiance

Given the above evidence that aerosol size distribution and composition varies widely, we consider a different measure of the aerosol that can be estimated from satellite measurements without any assumptions about the aerosol size distribution and composition. This dimensionless measure, which we call the aerosol radiance, is simply the difference between the radiance (normalized by the irradiance at the top of the atmosphere) measured by the satellite and an estimate of the radiance that would be measured in the absence of aerosol. It is a useful validation field because it can be estimated from satellite radiance measurements without any assumptions about the aerosol optical properties. In MIRAGE the aerosol radiance Ψ is defined in much the same way as satellite analysis [*Wagener et al.*, 1997]:

$$\Psi = \sum_{k=1}^{K} \tau_k \omega_k \left[P_k(\Theta_1) + \{\alpha(\theta_s) + \alpha(\theta_v)\} P_k(\Theta_2) \right]. \quad (13)$$

Here $P(\Theta_1)$ is the phase function for scattering of the direct beam toward the satellite viewing angle, $\alpha(\theta_s)$ is the reflectance of the direct beam at the surface, $\alpha(\theta_v)$ is the surface reflectance toward the satellite of the photons scattered once in the atmosphere, and $P(\Theta_2)$ is the phase function for the scattering once in the atmosphere and once at the surface. The surface reflectance is calculated for the solar zenith angle θ_s and satellite zenith angle θ_v using the same Fresnel reflection function used by *Wagener et al.* [1997]. The phase functions are calculated for each layer by interpolating between parameterized Mie calculations at a discrete set of 10 scattering angles ranging from 1.1 to 3.14 radians. The phase function at each of the 10 scattering angles is calculated from

$$P(\Theta) = \frac{\lambda^2}{4\pi\sigma_s} \int \left[|S_1(\Theta, r)|^2 + |S_2(\Theta, r)|^2 \right] n(r) dr, \quad (14)$$

using *Wiscombe*'s [1979] Mie code at the beginning of each simulation. Here λ is wavelength (0.64 μm), S_1 and S_2 are the Mie amplitude functions [*Liou*, 1992], $n(r)$ is the lognormal distribution of aerosol number concentration with size, and σ_s is the scattering coefficient for the same refractive index and size distribution. The dependence of the phase function on aerosol wet surface mode radius and wet refractive index is parameterized in the same way as the aerosol extinction

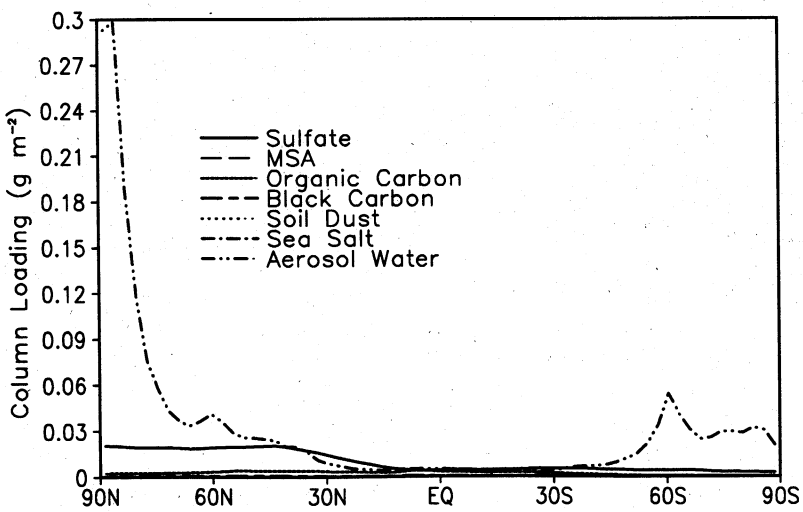

Figure 14. Zonal and annual mean column-integrated mass concentrations of each component of the aerosol simulated by MIRAGE for the accumulation mode.

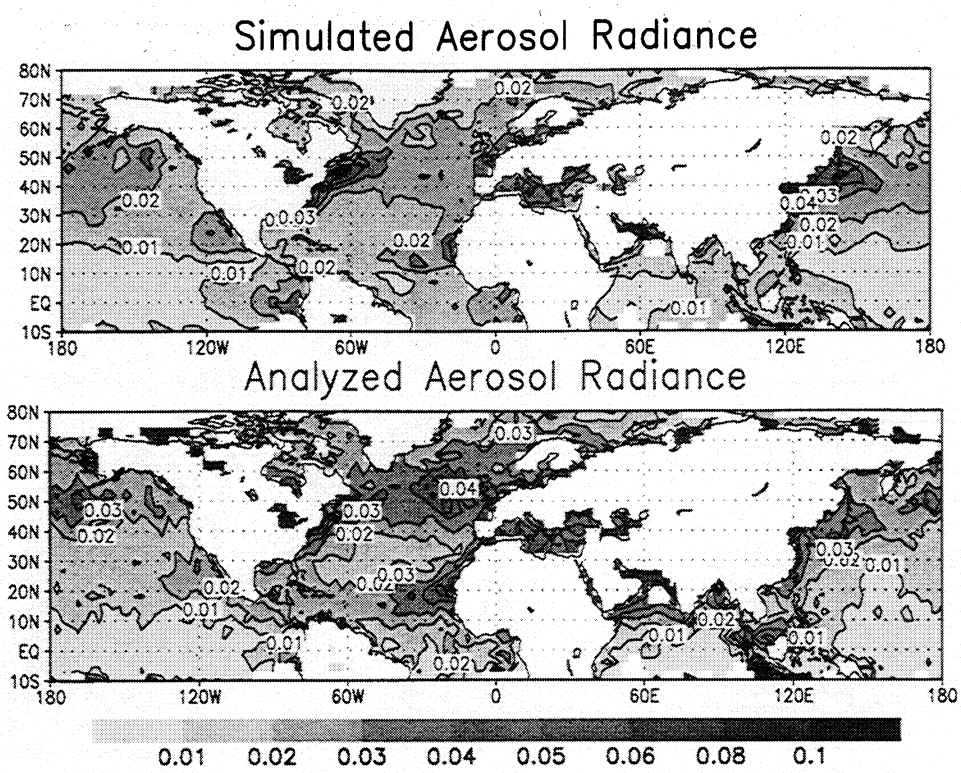

Figure 15. August 1994 mean aerosol radiance simulated by MIRAGE and estimated from AVHRR radiance measurements by *Wagener et al.* [1997].

coefficient. The aerosol radiance is only calculated for grid cells viewed by satellite, which is less than 100 each hour.

Figure 15 compares the simulated and observed aerosol radiance for August 1994. Many of the features evident in the comparison between simulated and observed aerosol optical depth are also evident for the aerosol radiance, but the relative biases in the simulated aerosol radiance are noticeably smaller than those for the simulated aerosol optical depth. Unfortunately, during this period, measurements of the aerosol radiance were not possible over the Southern Hemisphere, where the aerosol composition is quite different from that in the Northern Hemisphere. Moreover, at no time can the aerosol radiance be estimated over land, where the single-scattering albedo can be much lower than over the ocean. Thus aerosol radiance does not provide any more information about the MIRAGE performance than the aerosol optical depth. Evaluation for other periods, when global AVHRR (or, better yet, Multi-Angle Imaging Spectroradiometer (MISR)) coverage is available, will be necessary to determine whether the interhemispheric differences in aerosol composition are real and measurable.

3.8. Aerosol Direct Radiative Forcing

Finally, we evaluate the prediction of the direct radiative forcing by comparing the MIRAGE simulation with an analysis of aircraft and satellite radiance measurements by *Bergstrom and Russell* [1999]. Plate 2 compares the annual mean direct radiative forcing for the North Atlantic, as simulated by MIRAGE and as estimated by Bergstrom and Russell. Two estimates from observations are presented, one that neglects the effects of clouds on the direct forcing (i.e., the clear-sky forcing is applied even if clouds are present) and the other that neglects the direct forcing when clouds are present. The MIRAGE prediction of the direct forcing is based upon two calculations of the planetary radiation balance each time that radiation calculations are performed, one that accounts for the radiative scattering and absorption by the aerosol and the other that neglects them entirely. The direct forcing is determined from the difference between the two estimates of the radiative flux at the top of the atmosphere. By including the contribution of aerosol scattering above, below, and within clouds to the estimate of direct forcing, such a treatment will yield a stronger estimate of the radiative forcing than a treatment that neglects the direct forcing when clouds are present. By accounting for the scattering of sunlight by clouds above the aerosol, the treatment will yield a weaker estimate than one that neglects the effects of scattering by clouds on the direct forcing. As might therefore be expected, the MIRAGE estimate of the direct forcing is between the two estimates by Bergstrom and Russell. The simulated direct forcing by all aerosols in MIRAGE is -1 to -3 W m^{-2} across most of the North Atlantic, with the strongest forcing off the east coast of the United States and west coast of Africa. The estimate from radiance measurements is -3 to -6 W m^{-2} if the effects of clouds are neglected and zero to -2 W m^{-2} if the direct forcing is neglected when clouds are present.

4. Summary

A variety of measurements have been used to evaluate the treatment of aerosol radiative properties and radiative impacts of aerosols simulated by MIRAGE. Laboratory measurements have been used to evaluate the treatment of water

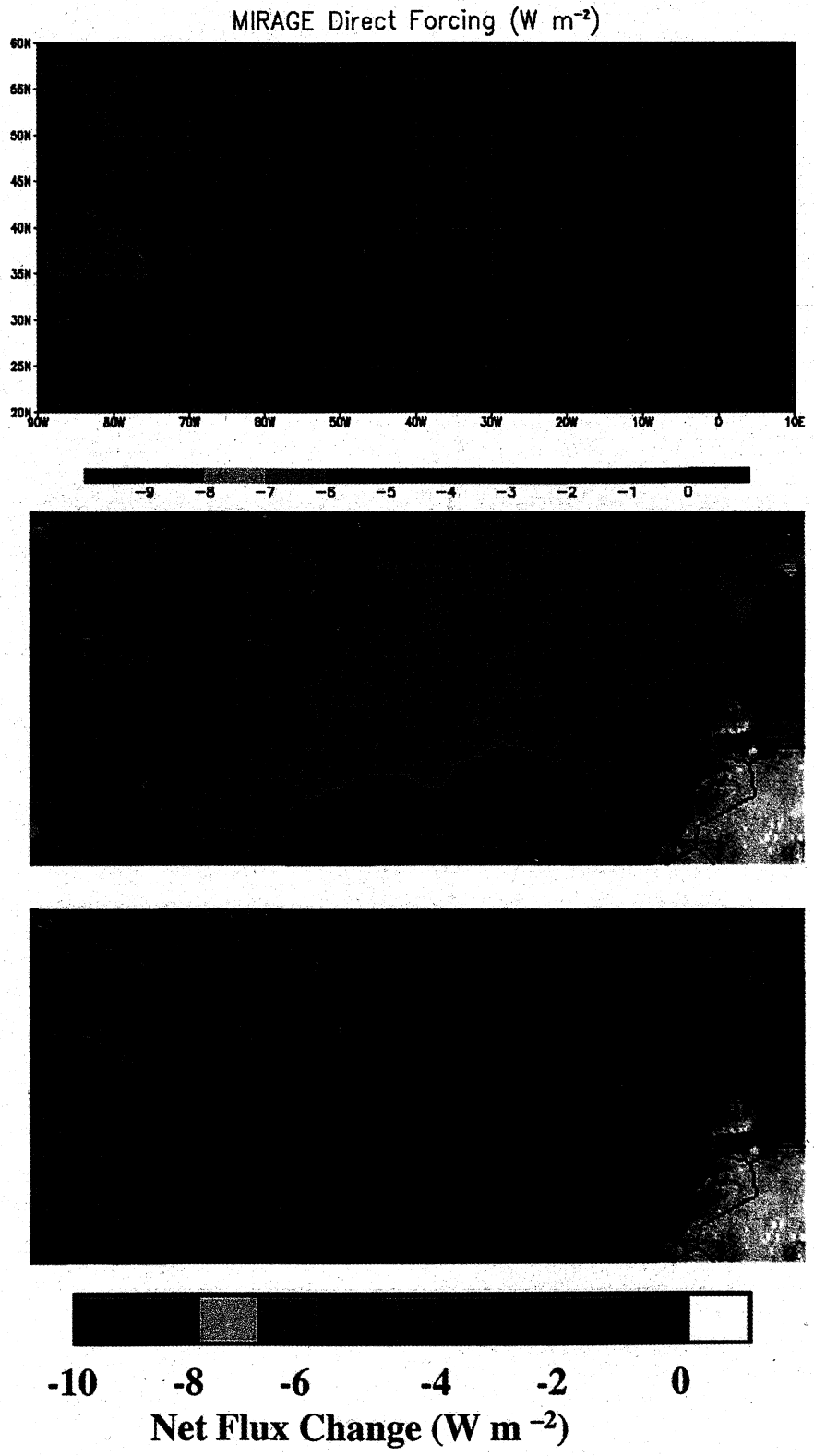

Plate 2. Annual mean direct radiative forcing by aerosol, as simulated by MIRAGE (top), as estimated by *Bergstrom and Russell* [1999] neglecting the influence of clouds (middle), and as estimated by Bergstrom and Russell neglecting the radiative forcing under cloudy conditions (bottom).

uptake in MIRAGE. ECMWF analyses of radiosonde measurements have been used to evaluate the simulation of relative humidity. Surface measurements of irradiance have been used to evaluate the simulation of aerosol optical depth. Two different analyses of satellite radiance measurements have been used to evaluate the global simulation of aerosol optical depth over the oceans. In situ surface measurements of aerosol single-scatter albedo have been used to evaluate the simulation by MIRAGE. Satellite estimates of the aerosol Ångström exponent have been used to provide information about the performance of the MIRAGE simulation of aerosol size distribution. Estimates of the sensitivity of radiative forcing to aerosol optical depth from radiance measurements have been compared with the MIRAGE simulation. Estimates of the impact of aerosols on the radiance measured by satellite have been compared with that simulated by MIRAGE. Finally, an estimate of the direct forcing by aerosols in the North Atlantic, based upon radiance measurements, has been compared with the MIRAGE simulation.

In many respects the simulation is found to be quite realistic. The treatment of water uptake in MIRAGE agrees quite well with laboratory measurements for the components for which measurements are available. The parameterization of aerosol radiative properties agrees with the Mie theory under a wide range of particle sizes. MIRAGE simulates the spatial distribution of aerosol optical depth rather well; under most conditions the simulated aerosol optical depth agrees with surface and satellite estimates to within a factor of 2. The simulated single-scatter albedo agrees with the range of measured values in the places that measurements are available. MIRAGE correctly simulates smaller particle sizes over and downwind from regions with primary emissions and secondary production of accumulation mode particles and larger particle sizes over and downwind from regions with emissions of coarse particles. The simulated sensitivity of radiative forcing to aerosol optical depth is consistent with estimates from measurements where available. The simulated spatial distribution of aerosol radiance is consistent with estimates from satellite measurements. The simulated direct forcing is within the uncertainty of estimates from measurements in the North Atlantic.

However, some serious problems have been identified. MIRAGE simulates relative humidity near 100% far too frequently, so in the simulation reported here, the ECMWF-analyzed relative humidity is used to estimate water uptake. Even so, the assumption of Köhler equilibrium to estimate water uptake is inappropriate for the coarse modes and should be replaced with a kinetic treatment in which aerosol water for the coarse modes is predicted rather than diagnosed. The simulated sensitivity of aerosol extinction to relative humidity is consistent with available in situ humidograph measurements in some regions but is overestimated in many others. MIRAGE simulates excessively high aerosol optical depths off the east coast of the United States and China and too little dust off the coast of West Africa and in the Arabian Sea (E2000). The simulated aerosol optical depth may be too high in the Arctic as well, but observations there are not yet available. Simulated aerosol optical depths are low over sites in Brazil during the biomass burning season and in central Canada during the wildfire season, which indicates problems with emissions of organic and black carbon from these sources.

Several features of the MIRAGE simulation are intriguing, but measurements are not available for verification. The low single-scattering albedo simulated over the ocean at latitudes 20°-50°S is unexpected; although TOMS measurements provide qualitative information about absorption by aerosols above the boundary layer [*Herman et al.*, 1997a], quantitative measurements of single-scatter albedo throughout the troposphere are clearly needed for the same period as the simulation to determine whether it is realistic. The radiative warming over the Arctic and Antarctic is certainly plausible, but again, measurements are needed there. The large optical depths simulated at latitudes 55°-65°S would be very difficult to verify because they are associated with cloudy conditions; we suspect they are unrealistic because MIRAGE assumes the aerosol water is in equilibrium with relative humidity, neglecting kinetic effects on growth.

Much more extensive evaluation of the simulated direct radiative forcing will be possible with the launch of the Earth Observing System and other satellites. The multispectral radiance measurements from MODIS [*Tanré et al.*, 1997], multiangle measurements from MISR [*Kahn et al.*, 1997], and polarization measurements from EOSP [*Mishchenko and Travis*, 1997], and POLDER [*Herman et al.*, 1997b] will provide global estimates of not only aerosol optical depth but also mean particle size. The planned PICASSO-CENA mission will provide profiles of aerosol backscatter and extinction below the path of the satellite orbit.

Appendix A: Surface Measurements of Aerosol Optical Depth

We have compiled a database of surface measurements of aerosol optical depth (AOD) at over 50 sites (Figure A1). Although the estimates of aerosol optical depth from surface radiance measurements are much more accurate than estimates from satellite measurements, the spatial distribution of surface measurements is far from complete, with a preponderance of sites in the United States and rather few elsewhere. Table A1 lists the names, locations, and operation period for each site. Aerosol optical depth has only been estimated for the period of the MIRAGE evaluation (June 1994 to May 1995). Estimates are not available under cloudy skies and when instruments malfunction.

Our primary source of data is from multifilter rotating shadowband radiometer (MFRSR) observations [*Harrison et al.*, 1994]. These are mostly confined to the continental United States, with a few sites distributed in Australia and Hawaii in the Pacific and in Barbados and Bermuda in the Atlantic Oceans, respectively. The MFRSR measures total and diffuse solar irradiance in six narrowband spectral intervals, nominally between 400 and 1000 nm. One of the channels (at 940 nm) is used for estimating column water vapor. With these two components and the cosine response of the receiver optics, the direct normal irradiance is easily calculated. *Harrison and Michalsky* [1994] describe how the total optical depth can be calculated from the direct beam irradiance using the Beer-Lambert-Bouguer law. AOD is then calculated from the total optical depth by subtracting the contribution of molecular (or Rayleigh) scattering, which is a well-defined function of pressure and temperature, and an estimated contribution from ozone absorption. The accuracy of the measurements is usually better than 0.01 optical depth

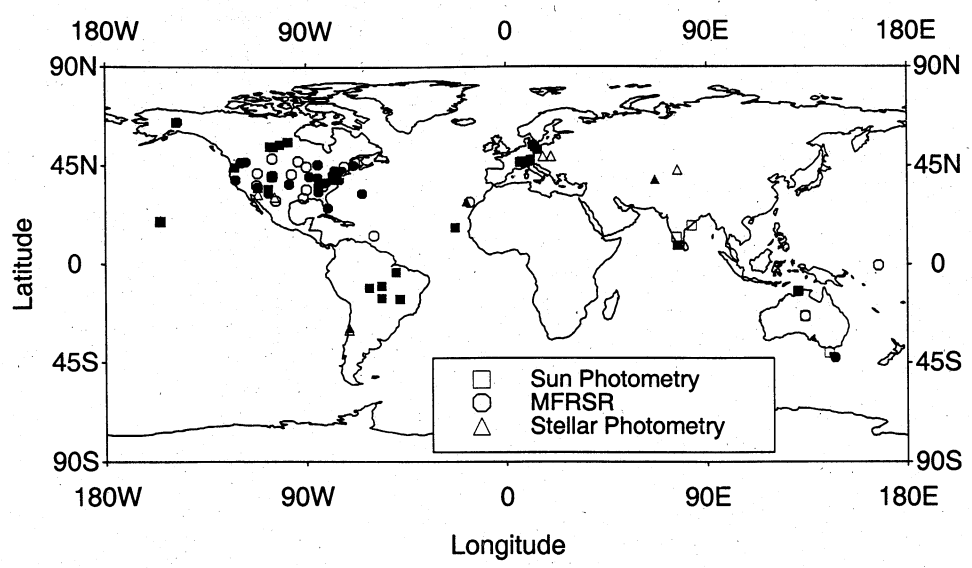

Figure A1. Locations of stations where surface measurements of aerosol optical depth are available. Solid symbols denote stations with aerosol optical depth available for the simulation period June 1994 to May 1995. Open symbols denote stations that provide measurements at other times.

Table A1. List of Sites with Available AOD Data Used in the Model Evaluation

Site	Lat.	Long.	Alt(m)	Data Date (yy.mm to yy.mm)	Source
Albany, New York	42.7	286.2	80	91.12 to present	3
Andrews Forest, Oregon	44.2	237.8	830	94.06 to 97.12	1
Bluefield, West Virginia	37.3	278.8	823	91.11 to present	3
Bonanza Creek, Alaska	64.7	211.7	150	94.05 to 97.10	1
Bondville, Illinois	40.0	271.6	213	91.12 to present	3
Burtonsville, Maryland	39.1	283.1	50	94.12 to 95.03	1
Davis, California	38.5	238.2	18	94.07 to present	2
Douglas Lake, Michigan	45.6	275.3	238	94.08 to present	2
Flagstaff, Arizona	35.2	248.3	2173	93.07 to present	11
Gaithersburg, Maryland	39.1	282.8	50	94.12 to 95.03	1
Geneva, New York	42.9	283.0	218	94.08 to present	2
Greenbelt, Maryland	39.0	283.1	50	93.05 to present	1
Griffin, Georgia	33.2	275.6	270	94.06 to present	2
Howland, Maine	45.2	291.3	67	91.10 to 95.11	3
Ithaca, New York	42.4	283.4	503	91.10 to 95.09	3
Jornada, New Mexico	32.6	253.3	1317	94.09 to present	2
Jug Bay, Maryland	38.8	282.2	10	94.11 to 95.03	1
Lamont, Oklahoma (CF-1)	36.6	262.5	318	92.06 to present	3
Lewes, Delaware	38.8	284.9	13	91.11 to present	3
Mauna Loa, Hawaii	19.5	204.4	3397	94.06 to present	1,11
Miami, Florida	25.7	279.9	10	94.05 to present	6
Oak Ridge, Tennessee	35.9	275.7	380	91.10 to present	3
Oxford, Ohio	39.5	275.3	286	91.11 to present	3
Pawnee, Colorado	40.8	255.2	1641	93.12 to present	2
Pine Grove Mills, Pennsylvania	40.7	282.1	375	91.10 to present	3
Pullman, Washington	46.7	242.8	804	94.07 to present	2
Richland, Washington	46.3	240.7	130	93.05 to present	11
RMO, Richland, Washington	46.4	240.4	1088	92.08 to present	11
SERC, Maryland	38.9	283.5	10	94.11 to 95.03	1
Sevilleta, New Mexico	34.4	253.1	1477	94.05 to 98.11	1
Boreas (NSA), Manitoba	55.9	261.7	290	94.05 to 96.10	1
Boreas (SSA), Saskatchewan	53.7	255.3	490	94.05 to 96.10	1
Flin Flon, Manitoba	54.7	258.3	305	94.05 to 95.11	1
Thompson, Manitoba	55.8	262.1	218	94.06 to 97.10	1
Waskesiu, Saskatchewan	53.9	253.9	550	94.05 to 98.11	1

Table A1. (continued)

Site	Lat.	Long.	Alt(m)	Data Date (yy.mm to yy.mm)	Source
Bern, Switzerland	47.0	7.4	560	92.03 to present	5
Davos, Switzerland	46.8	9.9	1590	91.01 to present	5
Hohenpeissenberg, Germany	47.8	11.0	985	93.11 to present	4
Jungfraujoch, Switzerland	8.0	3580		94.12 to present	5
Lindenberg, Germany	14.1	112		86.02 to present	4
Locarno-Monti, Switzerland	8.8	366		94.04 to present	5
Payerne, Switzerland	7.0	490		94.06 to present	5
Potsdam, Germany	53.4	13.0	104	94.11 to present	4
Zingst, Germany	54.4	12.1	12	87.04 to present	4
Samarkand, Uzbekistan	66.9	2540		82.07 to 95.11	10
Trivandrum, India	8.6	77.0	3	85.11 to present	7
Cape Verde	16.7	337.1	60	94.10 to 97.12	1
Alta Floresta, Brazil	-9.9	304.0	175	93.06 to 95.10	1
Brasilia, Brazil	-15.9	312.1	1100	93.06 to 95.11	1
Cuiaba, Brazil	-15.5	304.0	250	93.06 to 95.11	1
Ji Parana, Brazil	-10.9	298.2	100	94.08 to 95.10	1
La Serena, La Silla, Chile	289.3	2375		86.12 to present	8
Tukurui, Brazil	-3.7	310.3	100	93.07 to 95.10	1
Alice Springs, Australia	133.9	547		94.09 to present	11
Darwin, Australia	-12.4	130.9	32	94.09 to present	11
Hobart, Tasmania	-42.8	147.3	34	94.09 to present	11
Bermuda	32.4	295.3	10	94.07 to present	
La Palma, Canary Islands	342.1	2326		84.05 to 98.06	9

Source 1, AERONET (Aerosol Robotic Network); 2, USDA UVB Radiation Monitoring Program (MFRSR); 3, Quantitative Links Network and ARM SGP (MFRSR); 4, German Weather Service Sunphotometer Network; 5, Swiss Atmospheric Radiation Monitoring (CHARM) network, including the Swiss Optical Depth network; 6, University of Miami Sun photometer network; 7, Aerosol Climatology Project of the Indian Space Research Organization Geosphere Biosphere Program; 8, Geneva Observatory of the University of Geneva; 9, Institute of Astronomy at Cambridge University; 10, Sternberg Astronomical Institute of Moscow State University; 11, PNNL MFRSR.

units. Detailed processing of the MFRSR irradiance and total optical depth data has been carried out only for the sites listed in Table A1 for the 1994-1995 time period coinciding with the model simulations. Much more work is needed to process and screen the data for all sites and time periods to a level commensurate with that used in the model evaluation studies.

Other data sources are from direct solar beam measurements, obtained with handheld or Sun-tracking Sun photometers, and from stellar photometry. These data are reported either as total optical depth (TOD) or AOD, with analysis using the Beer-Lambert-Bouguer law already having been performed. The astronomical data, however, are reported as total atmospheric light extinction in units of magnitudes per air mass and so must be adjusted by a factor of about 0.92 to be consistent with AOD. The AOD data used in the model evaluation study are daily (or nightly) averaged values at a wavelength of 500 nm (or interpolated to 500 nm from about 550 nm for the astronomical values).

Acknowledgments. This study was primarily supported by the NASA Earth Science Enterprise under contract NAS5-98072 and grants NAG5-8797 and NAG5-9531. Support was also provided by the U.S. Department of Energy Atmospheric Radiation Measurement Program and Atmospheric Chemistry Program, both of which are part of the DOE Biological and Environmental Research Program. The Pacific Northwest National Laboratory is operated for the DOE by Battelle Memorial Institute under contract DE-AC06-76RLO 1830. Phillip Russell provided the estimate of direct radiative forcing from radiance measurements. Compton Tucker of NASA GSFC provided the AVHRR GAC data. Larry Stowe provided the NOAA analysis of aerosol optical depth. Brent Holben (NASA GSFC), along with several other investigators federated with AERONET, including Brian_Markham (NASA GSFC), John Vande Castle, and Didier Tanré (Univ. of Lille/CNRS/CNES), provided the AERONET data (see http://aeronet.gsfc.nasa.gov:8080/). James Slusser and Dave Bigelow of the Natural Resource Ecology Laboratory, Colorado State University, provided the USDA UVB Radiation Monitoring Network data (see http://uvb.nrel.colostate.edu/UVB/). Joe Michalsky (SUNY, Albany) provided the Quantitative Links Network and ARM SGP data (see http://hog.asrc.cestm.albany.edu/). Michael Weller (DWD, Potsdam) and Ulrich Leiterer (DWD, Lindenberg) provided the data from the German Weather Service Sunphotometer Network. Alain Heimo (Swiss Meteorological Institute, network operations), Chris Wehrli (World Radiation Center, Davos, instrument development and calibration), and Thomas Ingold (University of Bern, data analysis) provided the Swiss Atmospheric Radiation Monitoring (CHARM) network, including the Swiss Optical Depth Network, data. Ken Voss (University of Miami, network operations) and Michael Alexandrov (NASA GISS, data analysis) provided the University of Miami Sunphotometer network data. B. H. Subbaraya and K. Krishnamoorthy provided data from the Aerosol Climatology Project of the Indian Space Research Organization Geosphere Biosphere Program. Gilbert Burki of the Geneva Observatory (University of Geneva) provided astronomical atmospheric extinction data obtained at the European Southern Observatory at La Silla, Chile (see also *Burki et al.* [1995], *Astron. and Astrophys. Suppl. Ser. 112*, 383). Dafydd Wyn Evans of the Institute of Astronomy at Cambridge University provided atmospheric extinction data as determined by the Carlsberg Automatic Meridian Circle (CAMC) on the island of La Palma in the Canary Islands. Leonid Berdnikov of the Sternberg Astronomical Institute of Moscow State University provided atmospheric extinction data obtained at the Maidanak Astronomical Observatory. Nels Larson provided PNNL MFRSR data. Theodore Anderson of the University of Washington provided the single-scatter albedo data for Cheeka Peak.

References

Abdul-Razzak, H., and S. J. Ghan, A parameterization of aerosol activation, 2, Multiple aerosol types, *J. Geophys. Res., 105*, 6837-6844, 2000.

Anderson, T. L., and J. A. Ogren, Determining aerosol radiative properties using the TSI 3563 integrating nephelometer, *Aerosol Sci. Technol., 29*, 57-69, 1998.

Anderson, T. L., D. S. Covert, J. D. Wheeler, J. M. Harris, K. D. Perry, B. E. Trost, D. J. Jaffe, and J. A. Ogren, Aerosol backscatter fraction and single-scattering albedo: Measured values and uncertainties at a coastal station in the Pacific Northwest, *J. Geophys. Res., 104*, 26,793-26,807, 1999.

Bergstrom, R. W., and P. B Russell, Estimation of aerosol direct radiative effects over the midlatitude North Atlantic from satellite and in situ measurements, *Geophys. Res. Lett., 26(12)*, 1731-1734, 1999.

Bodhaine, B. A., Aerosol absorption measurements at Barrow, Mauna Loa, and the south pole, *J. Geophys. Res., 100*, 8967-8975, 1995.

Bond, T., T. L. Anderson, and D. Campbell, Calibration and intercomparison of filter-based measurements of visible absorption by particles, *Aerosol Sci. Technol., 30*, 582-600, 1999.

Carrico, C. M., M. J. Rood, J. A. Ogren, C. Neusüß, A. Wiedensohler, and J. Heinztenberg, Aerosol optical properties at Sagres, Portugal during ACE-2, *Tellus, 52B*, 694-715, 2000.

Charlson, R. J., D. S. Covert, and T. V. Larson, Observation of the effect of humidity on light scattering by aerosols, in *Hygroscopic Aerosols*, edited by L. H. Ruhnke and A. Deepak, pp. 35-44, A. Deepak, Hampton, Va., 1994.

Chylek, P., V. Srivastava, R. Pinnick, and R. T. Wang, Scattering of electromagnetic waves by composite spherical particles: experiment and effective medium approximations, *Appl. Opt., 27*, 2396-2404, 1988.

Chylek, P., G. Videen, D. Ngo, R. G. Pinnick, and J. D. Klett, Effect of black carbon on the optical properties and climate forcing of sulfate aerosols, *J. Geophys. Res., 100*, 16,325-16,332, 1995.

Clarke, A. D., Aerosol light absorption by soot in remote environments, *Aerosol. Sci. Technol., 10*, 161-171, 1989.

Deuze, J. L., M. Herman, P. Goloub, D. Tanre, and A. Marchand, Characterization of aerosols over the ocean from POLDER, *Geophys. Res. Lett., 26*, 1421-1424, 1999.

Feichter, J., and U. Lohmann, Can a relaxation technique be used to validate clouds and sulphur species in a GCM?, *Q. J. R. Meteorol. Soc., 125*, 1277-1294, 1999.

Ferman, M. A., G. T. Wolff, and N. A. Kelly, The nature and sources of haze in the Shenandoah Valley/Blue Ridge Mountains area, *J. Air Pollut. Control Assoc., 31*, 1074-1082, 1981.

Francis, P. N., P. Hignett, and J. P. Taylor, Aircraft observations and modeling of sky radiance distributions from aerosol during TARFOX, *J. Geophys. Res., 104*, 2309-2319, 1999.

Ghan, S. J., and R. C. Easter, Comments on "A limited-area-model case study of the effects of sub-grid scale variations in relative humidity and cloud upon the direct radiative forcing of sulfate aerosol," *Geophys. Res. Lett., 25*, 1039-1040, 1998.

Ghan, S. J., L. R. Leung, and Q. Hu, Application of cloud microphysics to NCAR CCM2, *J. Geophys. Res., 102*, 16,507-16,528, 1997a.

Ghan, S. J., L. R. Leung, R. C. Easter, and H. Abdul-Razzak, Prediction of droplet number in a general circulation model, *J. Geophys. Res., 102*, 21,777-21,794, 1997b.

Ghan, S. J., R. C. Easter, J. Hudson, and F.-M. Bréon, Evaluation of aerosol indirect radiative forcing in MIRAGE, *J. Geophys. Res.*, in press, this issue (a).

Ghan, S. J., R. C. Easter, E. Chapman, H. Abdul-Razzak, Y. Zhang, R. Leung, N. Laulainen, R. Saylor, and R. Zaveri, A physically based estimate of radiative forcing by anthropogenic sulfate aerosol, *J. Geophys. Res.*, this issue (b).

Goloub, P., D. Tanre, J. L. Deuze, M. Herman, A. Marchand, and F. M. Breon, Validation of the first algorithm applied for deriving the aerosol properties over the ocean using the POLDER/ADEOS measurements, *IEEE Trans. Geosci. Remote Sens., 37*, 1586-1596, 1999.

Harrison, L., and J. Michalsky, Objective algorithms for the retrieval of optical depths from ground-based measurements, *Appl. Opt., 33*, 5126-5132, 1994.

Harrison, L., J. Michalsky, and J. Berndt, Automated multifilter rotating shadow-band radiometer: An instrument for optical depth and radiation measurements, *Appl. Opt., 33*, 5118-5125, 1994.

Haywood, J. M., and K. P. Shine, The effect of anthropogenic sulfate and soot aerosol on the clear sky planetary radiation budget, *Geophys. Res. Lett., 22*, 603-606, 1995.

Haywood, J. M., V. Ramaswamy, and L. J. Donner, A limited-area-model case study of the effects of sub-grid scale variations in relative humidity and cloud upon the direct radiative forcing sulfate aerosol, *Geophys. Res. Lett., 24*, 143-146, 1997.

Hegg, D. A., J. Livingston, P. V. Hobbs, T. Novakov, and P. Russell, Chemical apportionment of aerosol column optical depth off the mid-Atlantic coast of the United States, *J. Geophys. Res., 102*, 25,293-25,303, 1997.

Heintzenberg, J., Measurement of light absorption and elemental carbon in atmospheric aerosol samples from remote locations, *in Particulate Carbon: Atmospheric Life Cycle*, edited by G.T. Wolff and R.L. Klimisch, pp. 371-377, Plenum, New York, 1982.

Heintzenberg, J., and C. Leck, Seasonal variation of the atmospheric aerosol near the top of the marine boundary layer over Spitsbergen related to the Arctic sulfur cycle, *Tellus, Ser. B, 46*, 52-67, 1994.

Herman, J. R., P. K. Bhartia, O. Torres, C. Hsu, C. Seftor, and E. Celarier, Global distribution of UV-absorbing aerosols from Nimbus 7/TOMS data, *J. Geophys. Res., 102*, 16,911-16,922, 1997a.

Herman, M., J. L. Deuze, C. Devaux, P. Goloub, F. M. Breon, and D. Tanré, Remote sensing of aerosols over land surface, including polarization measurements and application to POLDER measurements, *J. Geophys. Res., 102*, 17,039-17,050, 1997b.

Hignett, P., J. P. Taylor, P. N. Francis, and M. D. Glew, Comparison of observed and modeled direct aerosol forcing during TARFOX, *J. Geophys. Res., 104*, 2279-2287, 1999.

Hobbs, P. V., J. S. Reid, R. A. Kotchenruther, R. J. Ferek, and R. Weiss, Direct radiative forcing by smoke from biomass burning, *Science, 275*, 1776-1778, 1997.

Japar, S. M., W. W. Brachaczek, R. A. Gorse Jr., J. M. Norbeck, and W. R. Pierson, The contribution of elemental carbon to the optical properties of rural atmospheric aerosols, *Atmos. Environ., 20*, 1281-1289, 1986.

Kahn, R., R. West, D. McDonald, B. Rheingans, and M. I. Mishchenko, Sensitivity of multiangle remote sensing observations to aerosol sphericity, *J. Geophys. Res., 102*, 16,681-16,870, 1997.

Kaufman, Y. J., Remote sensing of fires and smoke in SCAR-B, *Eos Trans. AGU, 78(17)*, Spring Meet. Suppl., S71, 1997.

Kent, G. S., G. K. Yue, U. O. Farrukh, and A. Deepak, Modeling atmospheric aerosol backscatter at CO_2 laser wavelengths, 1, Aerosol properties, modeling techniques, and associated problems, *Appl. Opt., 22*, 1655-1665, 1983.

King, M. D., Y. J. Kaufman, D. Tanre, and T. Nakajima, Remote sensing of tropospheric aerosols from space: Past, present and future, *Bull. Am. Meteorol. Soc., 80*, 2229-2259, 1999.

Kotchenruther, R. A., and P. V. Hobbs, Humidification factors for aerosols from biomass burning in Brazil, *J. Geophys Res., 103*, 32,081-32,089, 1998.

Kotchenruther, R. A., P. V. Hobbs, and D. A. Hegg, Humidification factors for atmospherics aerosols off the mid-Atlantic coast of the United States, *J. Geophys Res., 104*, 2239-2251, 1999.

Leung, L. R., and S. J. Ghan, Parameterizing subgrid orographic precipitation and surface cover in climate models, *Mon. Wea. Rev., 126*, 3271-3291, 1998.

Li, Z., A. L. Williams, and M. J. Rood, Influence of soluble surfactant properties on the activation of aerosol particlels containing inorganic solute, *J. Atmos. Sci., 55*, 1859-1866, 1998.

Liou, K. N., *Radiation and Cloud Processes in the Atmosphere*, Oxford University Press, New York, 487 pp., 1992.

Liousse, C., J. E. Penner, C. Chuang, J. J. Walton, H. Eddleman, and H. Cachier, A global three-dimensional model study of carbonaceous aerosols, *J. Geophys. Res., 101*, 19,411-19,432, 1996.

Malm, W. C., J. F. Sisler, J. F. Huffman, R. A. Eldred, and T. A. Cahill, Spatial and seasonal trends in particle concentration and optical extinction in the United States, *J. Geophys. Res., 99*, 1347-1370, 1994.

McInnes, L., M. Bergin, J. Ogren, and S. Schwartz, Apportionment

of lightscattering and hygroscopic growth to aerosol composition, *Geophys. Res. Lett., 25*, 513-516, 1998.

Mishchenko, M. I., and L. D. Travis, Satellite retrieval of aerosol properties over the ocean using polarization as well as intensity of reflected sunlight, *J. Geophys. Res., 102*, 16,989-17,014, 1997.

Mishchenko, M. I., A. A. Lacis, B. E. Charlson, and L. D. Travis, Nonsphericity of dust-like tropospheric aerosols: Implications for aerosol remote sensing and climate modeling, *Geophys. Res. Lett., 22*, 1077-1080, 1995.

Nakajima, T., and A. Higurashi, A use of two-channel radiances for an aerosol characterization from space, *Geophys Res. Lett., 25*, 3815-3818, 1998.

Nishikawa, M., Environmental effects of Kosa aerosol, *J. Environ. Chem.* (in Japanese), *3*, 673-682, 1993.

Nishikawa, M., S. Kanamori, N. Kanamori, and T. Mizoguchi, Kosa aerosol as eolian carrier of anthropogenic material, *Sci. Total Environ., 107*, 13-27, 1991.

Ogren, J. A., R. J. Charlson, D. S. Covert, T. L. Anderson, and M. J. Rood, Measurements of aerosol single-scattering albedo: Implications of its observed variability on estimates of aerosol radiative forcing, paper presented at CNES workshop, Reduction of Errors in Aerosol Forcing of Climate, Meribel, France, January 19-22, 1999.

Press, W. H., S. A. Teukolsky, W. T. Vetterling, and B. P. Flannery, 963 pp., *Numerical Recipes*, Cambridge Univ. Press, New York, 1992.

Pruppacher, H. R., and J. D. Klett, *Microphysics of Clouds and Precipitation*, 954 pp., Kluwer Acad., Norwell, Mass., 1997.

Quinn, P. K., S. F. Marshall, T. S. Bates, D. S. Covert, and V. N. Kapustin, Comparison of measured and calculated aerosol properties relevant to the direct radiative forcing of tropospheric sulfate aerosol on climate, *J. Geophys. Res., 100*, 8977-8891, 1995.

Reid, J. S., P. V. Hobbs, R. J. Ferek, D. R. Blake, J. V. Martins, M. R. Dunlap, and C. Liousse, Physical, chemical, and optical properties of regional hazes dominated by smoke in Brazil, *J. Geophys. Res., 103*, 32,059-32,080, 1998.

Russell, P. B., J. M. Livingston, P. Hignett, S. Kinne, J. Wong, A. Chien, R. Bergstrom, P. Durkee, and P. V. Hobbs, Aerosol-induced flux changes off the United States mid-Atlantic coast: Comparison of values calculated from Sun photometer and in situ data with those measured by airborne pyranometer, *J. Geophys. Res., 104*, 2289-2307, 1999.

Satheesh, S. K., and V. Ramanathan, Large differences in tropical aerosol forcing at the top of the atmosphere and Earth's surface, *Nature, 405*, 60-63, 2000.

Schult, I., J. Feichter, and W. F. Cooke, Effect of black carbon and sulfate aerosols on the global radiation budget, *J. Geophys. Res., 102*, 30,101-30,117, 1997.

Sloane, C. S. Effect of composition on aerosol light scattering efficiencies, *Atmos. Environ., 20*, 1025-1037, 1986.

Snider, J. R., S. Guibert, and J. L. Brenguier, Lack of Closure Between Dry and Wet Aerosol Measurements: Results from ACE-2, paper presented at AIP 15th International Conference on Nucleation and Atmospheric Aerosols, Rolla, Missouri, August 6-11, 2000.

Stowe, L., A. M. Ignotov, and R. R. Singh, Development, validation, and potential enhancements to the second-generation operational aerosol product at the national Environmental Satellite, Data and Information Service of the National Oceanic and Atmospheric Administration, *J. Geophys. Res., 102*, 16,923-16,935, 1997.

Tang, I. N., and H. R. Munkelwitz, Water activities, densities, and refractive indices of aqueous sulfates and sodium nitrate droplets of atmospheric importance, *J. Geophys. Res., 99*, 18,801-18,808, 1994.

Tanré, D., Y. J. Kaufman, M. Herman, and S. Mattoo, Remote sensing of aerosol properties over ocean using the MODIS/EOS spectral radiances, *J. Geophys. Res., 102*, 16, 971-16,988, 1997.

Wagener, R., S. Nemesure, and S. E. Schwartz, Aerosol optical depth over oceans: High space and time-resolution retrieval and error budget from satellite radiometry, *J. Atmos. Oceanic Technol., 14*, 577-590, 1997.

Waggoner, A. P., R. E. Weiss, N. C. Ahlquist, D. S. Covert, S. Will, and R. J. Charlson, Optical characteristics of atmospheric aerosols, *Atmos. Environ., 15*, 1891-1909, 1981.

Wang, M., S. Bailey, and C. McClain, SeaWiFS provides unique global aerosol optical property data, *Eos Trans., AGU, 81*, 197-202, 2000.

Wiscombe, W. J., Mie scattering calculations: Advances in technique and fast, vector-speed computer codes, *NCAR Tech. Note, TN-140+STR*, 62 pp., 1979. (Available from NTIS, Springfield, Va., *NTIS PB 301388/AS*.)

E. Chapman, R. Easter, S. Ghan, N. Laulainen, and R. Leung, Pacific Northwest National Laboratory, Richland, WA 99352. (steve.ghan@pnl.gov)

S. Nemesure and R. Wagener, Brookhaven National Laboratory, Upton, NY 11973.

Y. Zhang, Atmospheric and Environmental Research, San Ramon, CA 94583.

(Received October 28, 1999; revised June 6, 2000;
accepted August 9, 2000.)